Available online at www.sciencedirect.com
SCIENCE DIRECT®
Coordination Chemistry Reviews 249 (2005) 229–253
COORDINATION CHEMISTRY REVIEWS
www.elsevier.com/locate/ccr

Review

Variable energy photoelectron spectroscopy: electronic structure and electronic relaxation

Edward I. Solomon*, Lipika Basumallick, Peng Chen, Pierre Kennepohl

Department of Chemistry, Stanford University, Stanford, CA 94305, USA

Received 29 August 2003; accepted 6 February 2004
Available online 21 April 2004

Contents

* Corresponding author. Tel.: +1-650-723-4694; fax: +1-650-725-0259.
E-mail address: edward.solomon@stanford.edu (E.I. Solomon).

doi:10.1016/j.ccr.2004.02.016

Abstract

Use of variable photon energy with polarization available from synchrotron radiation has revolutionized the use of photoelectron spectroscopy (PES) in the study of transition metal complexes. The intensity dependence of PES peaks allows their definite assignment, a quantitation of the covalent mixing of the metal and ligand valence orbitals over the entire valence band, and an experimental determination of electronic relaxation. The last effect is the change in electronic structure with ionization, which is found to be large for transition metal complexes. Variable energy PES (VEPES) provides a powerful method to study bonding and its change with ionization and this provides fundamental insight into redox processes in inorganic and bioinorganic chemistry.

Keywords: Photoelectron spectroscopy; Variable photon energy; Electronic structure; Electronic relaxation

1. Introduction

Modern photoelectron spectroscopy (PES) has been recognized for over three decades as a powerful spectroscopic method to elucidate the character of both inner-shell (core) and outer-shell (valence) electrons in molecular species. The photoelectric effect was discovered in 1887 by Heinrich R. Hertz, who showed that ultraviolet light changes the voltage at which various metal electrodes spark. Then, in 1905 Albert Einstein, building on Max Plank's concept that light is quantized explained the photoelectric effect. It was postulated that the energy required for ejection of a photoelectron was directly related to the binding energy of that electron (i.e. by conservation of energy). The spectroscopic utility of this phenomenon was only developed much later (in the 1960s), when it was noted that a photoelectron spectrum could be generated by using high-energy photons and accurately measuring the kinetic energy of the photo generated electrons. The energy and intensity of the peaks in the kinetic energy spectrum provide direct information on the electronic structure of the species being studied.

The kinetic energy of the photoelectron (E_k) is directly related to its initial state binding energy (E_b) through the Einstein expression of the law of conservation of energy as given in Eq. (1.1).

$$E_k = h\upsilon - E_b \tag{1.1}$$

This basic relationship directly relates the energy of peaks observed in a photoelectron kinetic energy spectrum with the binding energy of electrons in the initial molecule and thus provides a theoretical frame to correlate the PES spectrum with the molecular energy levels. The intensity of the peaks is determined from the electric dipole transition moment that connects the initial and final states (including the ejected photoelectron) and the incident photon ($\langle\Psi_f|r|\Psi_i\rangle^2$). Conventional high intensity sources used for PES (i.e. ultra high vacuum discharge tubes and X-ray anodes) provide discrete incident photon energies at high resolution but cannot be used to probe the photon energy dependence of PES spectra. These sources are therefore limited in their ability to extract detailed information from the photoionization cross-section (vide supra) of PES spectra. By contrast, synchrotron radiation sources are completely tunable over a large range of photon energies and surpass the intensity of conventional laboratory VUV and X-ray sources. Synchrotron-based PES thus give significant benefits by enabling variable photon energy experiments, which can allow unambiguous assignment of the photoionization spectra.

When the electron is ionized there can be a large change in electron repulsion in the resultant ion. Its remaining electron density then redistributes to compensate for the hole produced. This is electronic relaxation. The change in wave function of the relaxed final states relative to the initial state leads to intensity in more than one final state. This gives rise to satellite structure in the spectrum, which can then be used as a direct probe of the change in electronic structure upon ionization.

This review first provides a description of the experimental setup for synchrotron-based PES experiments (Section 2) as well as the methodological basis for detailed analysis of core and valence PES spectra for transition metal complexes (Section 3). The evaluation of electronic structure through PES is described (Section 4) with special emphasis on electronic relaxation, a phenomenon that plays a significant role in defining the redox properties of transition metal complexes. Recent applications from the literature are chosen (Section 5) to illustrate the power of synchrotron-based PES in elucidating the electronic structure of systems of interest in inorganic and bioinorganic chemistry. From this, it should become clear to the reader that synchrotron-based photoelectron spectroscopy can be a powerful probe of electronic structure and its change with ionization, and thus provides a unique perspective in defining and understanding the physical properties and reactivity of important systems in inorganic and bioinorganic chemistry.

2. Experiment and instrumentation

As described above, the photoelectric effect is key in photoelectron spectroscopy and the PES experiment involves the measurement of the kinetic energy of the electron ejected due to incident radiation. The ionization energy, intensity as a function of photon energy and angular distribution of the emitted electrons are evaluated to obtain insight into the electronic structure of molecules.

2.1. Synchrotron radiation for photoelectron spectroscopy

Traditionally, the two most common sources of radiation used in photoelectron spectroscopy have been vacuum ultraviolet radiation (ultraviolet photoelectron spectroscopy, UPS) and X-rays (X-ray photoelectron spectroscopy, XPS) [1–6]. VUV radiation is primarily for the valence electrons and is characterized by high resolution (∼0.01 eV), which even resolve vibrational structures in the PES spectrum [7]. The source is usually the He(I) resonance line [4] at 21.2 eV or the He(II) line [8] at 40.8 eV. They are generated by the discharge through helium gas. With X-rays it is possible to study both core and valence electrons, although the resolution for X-rays is low (∼0.5 eV). The two most widely used sources are Mg Kα and Al Kα radiation generated in an X-ray anode with energies of 1253.6 and 1486.6 eV, respectively. These traditional sources provide high intensity but only at certain characteristic energies.

The evolution of synchrotron-based sources has bridged the gap between the low-energy (VUV) and high-energy (X-ray) regions and provided new opportunities for high-energy spectroscopy. Synchrotron radiation is the continuum of radiation (∼600 to ∼4 Å) produced by accelerating free electrons in a magnetic field. Synchrotron radiation has a number of characteristic properties that make it quite a unique tool for PES experiments [9,10] over earlier sources such as gas discharges or X-ray anodes. Tunability and broad spectral range allow a continuous spectrum from the infrared to the X-ray region. Its high intensity due to the high current accumulated in the storage rings is extremely important for various applications. The high brilliance—because of the small cross-section of the electron beam, the high degree of collimation of the radiation, and the high polarization (both linear and circular) have a variety of applications.

Tunability of the source enables the user to select a wavelength most appropriate for the experiment and has made it possible to optimize the photoionization cross-section and the electron escape depth. It has also added new dimensions to the traditional PES technique, in particular—variable energy photoelectron spectroscopy (VEPES), constant initial state (CIS) and constant final state (CFS) spectroscopy. The high degree of polarization is extremely useful for angle resolved photoemission (ARPES) applications where both the kinetic energy and the momentum distributions of the photoelectrons can be measured.

The description of a synchrotron radiation source has been presented in the Preface of this issue. Here, we describe how the synchrotron is used as a radiation source for PES experiments. Photon beam ports are provided along the ring to utilize the synchrotron radiation. The radiation generated is taken from the ports and delivered to the experimental stations through a beamline. A beamline typically has a set of valves (manual valve, fast-closing valve, gate valve, pneumatic valve, and beam shutters) to isolate the vacuum between the beam line and the ring in the event of equipment failure or experimental error at the beamline or for beam line maintenance. Monochromators and reflection mirrors are set up in the beam line according to the purpose and characteristics of the radiation to be used in an experiment.

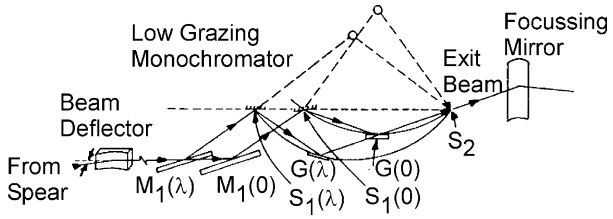

Fig. 1. Grasshopper monochromator.

Specialized monochromators are available for each of the VUV and X-ray regions of the spectrum. Monochromators for the UV region use gratings. Normal incidence monochromators [11] are used for lower photon energies and grazing incidence [12,13] for higher energies. The grazing-incidence grating type "grasshopper" monochromator designed by F.C. Brown and collaborators at the Stanford Synchrotron Radiation Laboratory [12,14] is shown in Fig. 1. It uses a combination of a spherical platinum coated quartz mirror (M), an entrance slit (S1), a gold grating (G) and an exit slit (S2) to provide monochromatic radiation from 32 to 1200 eV. Monochromators for the X-ray region use diffraction from crystals like Si, Ge, graphite, alumina, quartz etc. These crystals have rapid tunability over a broad spectral range, high transmission, narrow bandwidth and almost constant exit beam position and direction.

Mirrors are used for deflecting, focusing and filtering the beam: (i) beam splitting mirrors split/deflect part of the tangential radiation so that several experimental stations can share a single beam line. (ii) Spherical or toroidal mirrors are used in focusing the beam at a definite location of interest. (iii) Mirrors with sharp reflectivity cutoff are used to filter out certain photon energy. The reflectivity is determined by the angle of incidence, the photon energy, the mirror material and smoothness. Typically, mirrors should be ultra high vacuum, high temperature and high radiation level compatible and stable for years. Substrates for mirrors are typically Be, Cu, fused SiO_2, SiC, glass, etc. and the coating is usually Au or Pt although uncoated mirrors are also used. An issue for high-energy beam lines is that of thermal loading, which is minimized by using cooled metal mirrors.

2.2. Experimental setup

2.2.1. The chamber

The most important feature of the sample chamber used for photoemission work is the ability to maintain ultra high vacuum (UHV), which is defined as base pressure $\leq 5 \times 10^{-9}$ Pa. UHV is required because the chamber is directly open to the beam line and the ring during an experiment. Furthermore, maintaining UHV conditions increases the mean

free path of electrons, ions and photons, removes adsorbed gases from the sample, prevents sample and detector contamination, and prevents electrical arcing. For obtaining and maintaining UHV it is necessary to have a chamber that can be sealed properly and have pumps, which operate efficiently at very low pressures. Before use, vacuum chambers are generally heated to ∼375 K ('baked') under mechanical and turbo pumping for 24–48 h to desorp gases inside the chamber. To survive this process, vacuum chambers are typically made of stainless steel with strong glass ports and ceramic parts for insulation. All joints are precision welded and flanges are sealed with metal (usually copper) gaskets that seal the joint under mechanical stress (by bolting the flanges together). A new gasket is needed every time the seal is broken and resealed.

There are three major classes of UHV pumps. Ion pumps work on the principle of gas molecule ionization and trapping. The ionization is the result of high-energy electrons traveling between a Ti cathode and a stainless steel anode. Magnets are appropriately placed in order to maximize the electron paths. Ionized gases are accelerated toward the cathode and they collide, implanting or chemically reacting with the Ti cathode. Diffusion pumps work on the principle of momentum transfer between a stream of moving vapor and residual gases in the vacuum chamber. The vapor is condensed and reheated, and this is cyclically repeated. Silicones or polyphenyl ethers having low vapor pressure are generally used in diffusion pumps. Cryopumps, as the name suggest, condense and trap gases at very low temperatures. These pumps use closed He circuits to cool the pumping core to 30–50 K. The pumping core contains a cryosorbant material (typically charcoal or zeolite) to trap the gases.

Additionally, UHV systems require sample entry locks with rough pumps that provide a way to insert/remove samples from the UHV chamber without severely disrupting the controlled atmosphere (in a manner analogous to antechamber systems for controlled-atmosphere glove boxes). The most commonly used rough pumps are conventional mechanical pumps and turbo-molecular pumps, which operate via a high-speed turbine. To further remove any reactive gases, UHV chambers are often equipped with titanium sublimation pumps (TSP). Sublimated Ti from a hot Ti–W filament is extremely reactive with water vapor, O_2, CO, H_2 and other reactive gases. The pressure in the chamber is lowered through formation of very stable titanium compounds. A schematic of an experimental chamber with some of the basic components is shown in Fig. 2. Another important component of the PES set up is the sample manipulator. It enables us to orient the sample at the desired angle with respect to the incident radiation and the detector.

2.2.2. Energy analyzer

The energy analyzer is the most important component of the experimental setup. This is where the photoelectrons are separated according to their kinetic energies. The early analyzers used for PES experiments were the retarding field

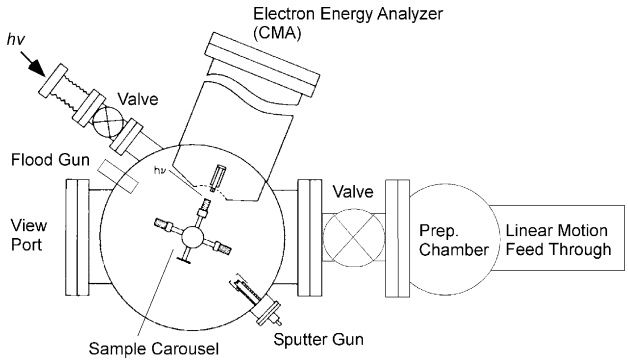

Fig. 2. Schematic of a PES beamline setup.

type [15,16]—cylindrical or spherical grids on which the potential is varied such that only electrons having energies greater than the retarding potential reach the detector. The other kind of analyzer commonly used in PES is the deflection analyzer, [17], which uses electric or magnetic fields to focus electrons according to their kinetic energies. Two basic designs are discussed herein: the hemispherical analyzer (Fig. 3A) and the cylindrical mirror analyzer (Fig. 3B).

The hemispherical analyzer consists of two concentric metallic spheres with an entrance slit and retarding grid at one end and an exit slit and electron multiplier at the other. There are two modes of operation—the constant analyzer energy and the constant retard ratio mode. If ΔV is the voltage difference between the two spheres, the energy that an electron must have in order to pass through the analyzer without colliding with it or the exit slit is called the pass energy (PE). It is related to the applied voltage as given in Eq. (2.1), where H is a geometric factor related to the separation of the hemispheres.

$$\mathrm{PE} = H\,\Delta V \tag{2.1}$$

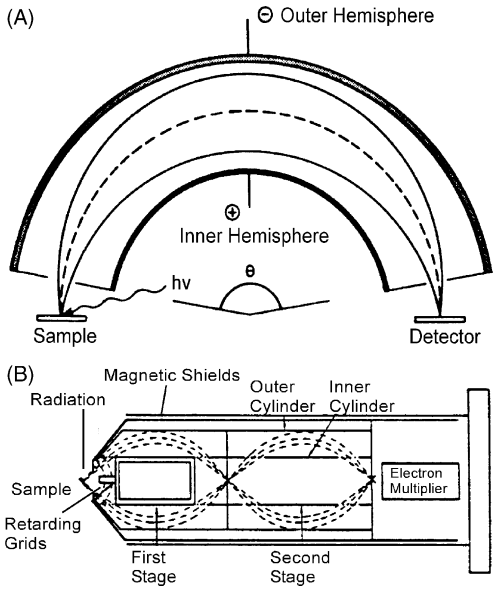

Fig. 3. (A) Hemispherical analyzer, (B) double-pass cylindrical mirror analyzer.

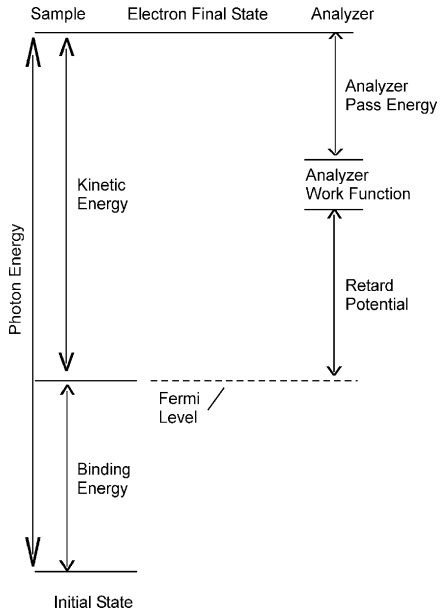

Fig. 4. Energy diagram.

In some applications it is desirable to have a single PE for all electrons coming from the sample. In order to do this, the retarding grid is used. The voltage on the grid is adjusted to accelerate or decelerate the electrons, which one wants to pass through the analyzer. The kinetic energy of an electron passing through the analyzer can be written as given in Eq. (2.2), where R is the voltage on the grid and W is the work function of the spectrometer (E_k is with respect to the Fermi level of the sample, Fig. 4). As the PE remains constant this mode is the constant analyzer mode. In certain applications (e.g., Auger data collection) the constant retard mode is used. In this mode, PE varies with kinetic energy. The retard ratio is defined as (PE + R)/(PE). A scan in this mode will have the energy resolution better at low E_k and count rate better at high E_k.

$$E_k = R + \mathrm{PE} + W \tag{2.2}$$

The cylindrical mirror analyzer (CMA) has two coaxially arranged cylinders, where the inner cylinder is typically held at ground potential and the outer cylinder has a negative voltage which is ramped to scan the desired energy range. The CMA can also be operated in the two modes described above. A double pass CMA, which contains two CMA segments in series, is commonly used for PES experiments. On entering the first segment, photoelectrons are deflected by a radial electric field between two coaxial cylinders and brought to a focus and energy resolved. The photoelectrons then enter the second segment, undergo the same deflection, are refocused and then detected. This double focusing of electrons greatly improves energy resolution since the second segment acts as a secondary photoelectron filter. The enhanced resolution is especially important when studying samples with rough surfaces and gas phase spectroscopy where the sample has a finite volume.

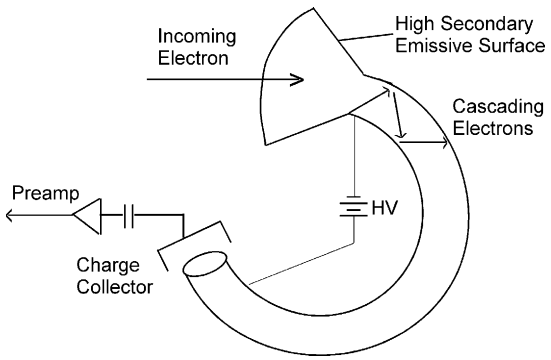

Fig. 5. Schematic of channeltron.

2.2.3. Detector

After passing though the analyzer the electrons reach the detector. Electron multipliers [18] (Fig. 5) are used to detect the electron fluxes. Commonly, an electron channel multiplier (channeltron) is used to detect the electrons and standard techniques are used for pulse counting. A channeltron is a horn-shaped continuous dynode structure that is coated on the inside with an electron emissive material. A voltage of ~2 kV is applied across the tube and a charged particle striking the channeltron creates secondary electrons that have an avalanche effect to create more secondary electrons and finally a current pulse. The gain is typically 10^9 and it decreases with age and continuous high voltage (>3.2 kV) or significant pressure rise in the chamber. The signal produced by the multiplier is directed to the counting equipment, where pulses are counted digitally.

2.2.4. Electron flood gun

Many materials generate a strong surface potential when exposed to X-rays. This effect is more prominent with monochromatic sources. The surface charge developed is due to the difference in the electron loss from the surface though emission and electron gain by conduction. In order to maximize sensitivity and resolution of the PES spectrum this charge must be reduced to a minimum, and be uniform in nature. A variable surface charge results in differences in peak energy and reduces the energy resolution of the experiment. Surface charging is also influenced by surface roughness and contamination. The conventional method for compensating for the positive charge build up involves the use of a focused electron gun, which supplies a highly uniform flux of low-energy electrons to the surface.

2.2.5. Other features

The main vacuum chamber is usually connected to a pre-chamber via a gate valve for sample preparation and transfer. The gate valve is capable of holding high vacuum conditions when open to atmospheric pressures on one side. The sample is loaded in the pre-chamber, pumped down to medium vacuum and then the gate valve is opened allowing the sample to be inserted into the UHV chamber. UHV conditions are quickly restored in the main chamber. There

exist a wide range of transfer mechanisms to get the sample from the pre-chamber into the main chamber.

In many cases, a gas manifold consisting of a reservoir, suitable pressure regulators, gauges and valves, are used to introduce gases into the vacuum chamber under controlled conditions. The sample holder in the main chamber is also often equipped with heating and cooling mechanisms to regulate sample temperatures. The ion gun is another useful accessory, which provides the ability to ion sputter the sample for cleaning. Ion guns work by ionizing a gas and then accelerating and focusing the beam of ions onto the sample.

2.3. Sample requirements

Solid-state PES is very surface sensitive because of the limited mean-free path of the electrons (of the order of 10 Å). Thus, sample preparation (both outside and within the UHV chamber) is very important for a PES experiment. A 'clean' sample is required to obtain high quality PES data. In general, the sample, its holder and the substance that secures the sample to the holder should be UHV compatible. The preparation of the sample depends on the history of the sample, the kind of surface analysis that will be done and the vacuum level in the chamber. All materials that are introduced into the chamber needs to be handled with clean and demagnetized tools. Samples are attached to the holder either mechanically using screws, metal clips or by UHV compatible cement, silver epoxy or methanol 'dag' (a colloidal suspension of graphite particles in methanol). Solid samples must be grounded to neutralize surface charges. Usually, in the case of solids, it is cleaved under vacuum immediately prior to the experiment, to expose a clean surface. Techniques like ion sputtering, annealing are also used to clean the sample surface. These processes are used separately or in combination to get atomically clean and ordered surfaces. For example, light ion sputtering can be done to clean surface contaminants followed by heating to re-crystallize the ion-damaged surface. PES can also be done on gaseous samples, where the sample is generated in the gas cell. Differential pumping is used to isolate the high pressure of the gas cell from the beam line.

2.4. Nature of spectrum

PES is a photon in-electron out experiment, monochromatic photons are absorbed by the sample, and the excited electrons, which leave the surface, are analyzed with respect to their kinetic energy. The typical PES spectrum is a continuous record of electron count, integrated over a time constant (typically 1 s), plotted as a function of electron kinetic energy and is normalized to the incident photon flux. This is because the absolute counts are the result of a number of experimental variables—intensity of incident radiation, size and direction of the solid angle of collection, type of energy analyzer, surface charges on the sample, sensitivity of the electron detector, slit widths and residual magnetic fields in the chamber. Relative intensities represent the relative probabilities of photoionization and are reported in arbitrary units. PES data are normally reported in terms of the binding energy (e.g., Fig. 6) of the photoelectrons, as calculated from Eq. (1.1). This approach yields reasonable relative binding energies; absolute binding energies are obtained through direct calibration using an internal reference standard.

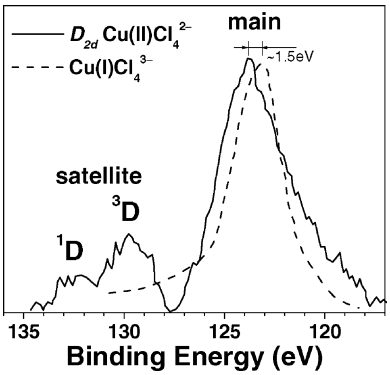

Fig. 6. PES spectra of Cu 3s core level in D_{2d} $[Cu(II)Cl_4]^{2-}$ and $[Cu(I)Cl_4]^{3-}$ (taken from reference [19]).

2.4.1. Constant initial state (CIS) spectroscopy

In constant initial state spectroscopy the energy distribution of electrons originating from a specified level (i.e. constant initial state) is recorded as the incident photon energy is scanned. As the photon energy is scanned, the energy difference between the incident photon and the electron analyzer is kept fixed, implying that the initial state of the photoelectrons is fixed and the final state is scanned. Thus, a CIS spectrum (e.g., Fig. 12 top) is a mapping of the final states, i.e. the density of unoccupied states.

2.4.2. Constant final state (CFS) spectroscopy

In constant final state spectroscopy the energy distribution of the electrons from any initial level, which have been photo excited to a specified final state is recorded as a function of the incident photon energy. The photon energy is scanned and the electron analyzer is held at a fixed energy. The CFS spectrum (e.g., Fig. 12 bottom) is a mapping of the initial states, i.e. the density of occupied states.

3. Spectroscopic methodology

In this section, we will review the methodology and various techniques of variable-energy photoelectron spectroscopy mainly using copper chlorides as examples. As mentioned above variable-energy PES can be conveniently subdivided into two sub-fields according to the orbital energy levels probed by the tunable-energy photons from the synchrotron radiation. The core level PES excites electrons from the atomic core levels, e.g., Cu 2s, 2p, and Cl 2s, 2p for copper chlorides. Valence level PES probes the

valence level electrons of the complexes, e.g., Cu 3d, Cl 3s, 3p. These two types of PES complement each other and provide a full spectrum of electronic information about inorganic metal complexes.

3.1. Core level PES

The high photon flux and high energy resolution of the synchrotron radiation give high signal intensity and resolution in core level PES compared to those provided by conventional X-ray sources (commonly termed XPS using Mg and Al X-ray anodes). The core electron binding energies of metal complexes determined by the PES experiment are characteristic of the specific elements in the complexes, and generally found to shift to deeper binding energies with increasing oxidation state of the atom. This binding energy increase is known in core level PES as a chemical shift and can be used to determine the oxidation state or charge density (i.e. Z_{eff}, effective nuclear charge) on an atom in a molecule [2]. Taking the 3s core level in $[CuCl_4]^{2-}$ as an example (Fig. 6), reduction from Cu(II) to Cu(I) results in a shift of ~1.5 eV to lower binding energy for the main photoelectron peak [19,20]. Note that binding energies must be corrected for the effect of electronic relaxation, which leads to the presence of satellite peaks as described below. In the presence of satellite peaks, the binding energy is given as the intensity weighted ionization energy in the sudden approximation (vide infra). Note that the intensity of the satellite peak is exhibited by and characteristic of the Cu(II) state. This shifts the intensity weighted average binding energy higher relative to the main peak for the Cu(II) complex.

A common feature in the core level photoelectron spectrum of open shell metal complexes is the additional satellite peaks accompanying the main photoelectron peak, which is observed in the Cu 3s PES spectrum of $[Cu(II)Cl_4]^{2-}$ at ~7 eV to deeper binding energy (Fig. 6). In the photoemission process of the Cu(II) complexes, an electron is ionized from a core level. The core hole leads to an increased effective nuclear charge. In order to compensate this, the initial metal-based half-occupied valence orbitals become more ligand-like while the initially filled valence ligand orbitals become more metal-centered (Scheme 1, middle). This corresponds to the main peak in Fig. 6. The resultant N-1 electron ion can further relax to give a higher energy satellite, which corresponds to a simultaneous core level photoemission and metal-to-ligand charge transfer "shake-up" transition (Scheme 1, right). While this is formally a two-electron process and the electric dipole moment operator can induce only one-electron transitions, the satellite transition becomes allowed through the change in wavefunction [19,21]. Thus, the satellite feature is a charge transfer transition of the one-electron ionized metal complex with the appropriate symmetry for configuration interaction (CI) mixing with the main peak (i.e. the same symmetry as the state corresponding to the main peak). As the symmetry of this shake-up transition (same as the initial structure) will generally be different from that allowed in electronic absorption spectroscopy, satellite structure provides a complementary low-resolution probe of metal–ligand bonding.

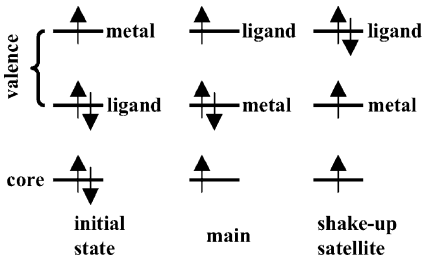

Scheme 1. Schematic description of core ionization and satellite formation: left, initial state; middle, resultant lowest energy final state associated with the main PES peak after ionization of a core electron; right, excited final state associated with the satellite.

The final state of the satellite peak in Fig. 6 has one unpaired electron in the Cu 3s level ($s = 1/2$) and one unpaired electron ($s = 1/2$) in the half-occupied metal d-based valence orbital (Scheme 1, right). These two electrons can couple and interact through electron repulsion to produce a singlet (^1D) and a triplet (^3D), with a multiplet intensity ratio of ~1:3 (Fig. 6). Their energy splitting is given by the Van Vleck expression (Eq. (3.1)) for photoemission from a filled s level, where S is the spin of the ground state, l is the orbital angular momentum of the valence shell and $K(s, l)$ is the exchange integral [22,23]. Thus, this multiplet splitting of the 3s level satellite gives a direct quantitative measure of the exchange interaction of a 3d electron with the 3s core. This interaction is also responsible for the spin polarization of core electrons which produces the isotropic contribution to hyperfine splitting (indirect Fermi contact) in the EPR spectrum of copper complexes [19]. For the final state of the main 3s photoelectron peak in Fig. 6, the multiplet coupling is between a Cu 3s electron and a ligand valence electron (i.e. over two different atoms, Scheme 1, middle). This multiplet splitting is small compared to that of the satellite and only contributes to the unresolved broadening of the main peak.

$$\Delta E = \frac{2S+1}{2l+1} K(s, l) \tag{3.1}$$

3.2. Valence level PES

Valence level electrons can also be probed using high energy photons as used in the core level PES, however, this can be accomplished at higher resolution using much lower energy photons in the vacuum ultraviolet region. This is traditionally performed using a dc (or microwave) discharge source (e.g., He(I) and He(II) lines), and termed ultraviolet photoelectron spectroscopy (UPS). Synchrotron radiation provides high intensity, high resolution and tunable energy photons from 20 to >300 eV. Since the PES selection rules allow ionization from all molecular orbitals, the binding energies of valence level electrons (e.g., Cu 3d and Cl 3p in

copper chlorides) can provide a direct one-electron energy level diagram of the metal complexes using Koopmans' theorem [24]. (The breakdown of Koopmans' theorem will be discussed later.) This is particularly useful for metal complexes such as Cu(I)Cl_4^{3-} where electronic absorption spectroscopy is limited due to the d^{10} configuration. Thus, PES is a powerful spectroscopic technique for studying bonding interactions in closed-shell systems.

3.2.1. Angular dependence

In addition to the binding energies of PES peaks, the intensity profiles of a photoelectron peak as a function of angular distribution detection and input photon energy also provide geometric and electronic structure information. The intensity of a photoelectron peak is determined by the photoionization cross-section $\sigma_{if}(E_k)$ for ejection of an electron with kinetic energy, E_k, from the *nl* subshell,

$$\sigma_{if}(E_k) = \frac{4\pi^2\alpha a_0^2}{3g(h\upsilon)}\left[\int \Psi_i r \Psi_f \, d\tau\right]^2 \quad (3.2)$$

where α is the fine structure constant (1/137), a_0 the Bohr radius (0.529 Å), g the number of degenerate subshells, and $h\upsilon$ is the input photon energy (in Rydberg). The term in brackets, which governs the intensity, is the electric dipole transition moment integral for a transition from the ground state (referred to as the initial state Ψ_i) to the excited state (the final state, Ψ_f). In PES, Ψ_f includes both the ionized complex and the outgoing photoelectron. Assuming no orbital relaxation, the transition dipole moment integral involves only the wavefunction of the electron before (Φ_i, bound state) and after (Φ_f, continuum function) ionization. Photoionization cross-sections are normally treated on an atomic level, where both Φ_i and Φ_f are described by spherical harmonics with separable radial functions (initial orbital $\phi_{n,l,}m_l$; photoelectron $\Phi_{E_k,l',}m_l$).

For the angular parts of the wavefunction, the selection rules which derive from the electric dipole operator in Eq. (3.2) require that $l' = l \pm 1$. These are referred to as photoionization channels and the $l + 1$ channel is usually the dominant process. Hence, photoemission of an electron from a d orbital will produce an *f* state continuum wavefunction. This in turn will produce an angular distribution ($d\sigma/d\Omega$) in the photoionization cross-section which can be detected through angle resolved photoelectron spectroscopy [25–27]. The theoretical angular distribution for a photoelectron emitted from a Cu $3d_{x^2-y^2}$ orbital by *z* polarized light with $h\upsilon = 40$ eV is shown in Fig. 7 [25]. Knowledge of these characteristic angular distribution (for example, in studies of chemisorbed small molecules on single crystal surfaces) has provided important geometric structure insight [25–30].

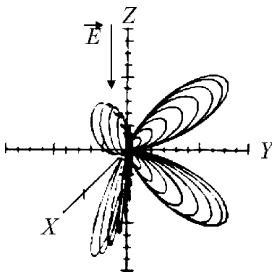

Fig. 7. Angular distribution of photoemission from a Cu $3d_{x^2-y^2}$ orbital: *z* polarized light with $h\upsilon = 40$ eV. The three-dimensional plot in one quadrant is shown, but the full four quadrant cross-section can be obtained by reflection in the *xz* and *yz* planes (taken from reference [25]).

3.2.2. Photon energy dependence

In addition to angular variation, the photoionization cross-section in Eq. (3.2) also changes significantly with input photon energy as determined by the radial wavefunctions of the initial and final states [31–33]. As the photon energy increases, the kinetic energy of the ejected electron also increases (KE = $h\upsilon$−BE). This causes the radial wavefunction of the continuum state to change in a manner, which can be qualitatively described by the free electron's de Broglie wavelength ($\lambda_e(\text{Å}) = 12.3/\sqrt{E_k(\text{eV})}$) as shown in Fig. 8. Quantitatively, the radial wavefunction for Φ_f is obtained by solving the radial Schrödinger equation, which significantly modifies the continuum wavefunction (relative to a free electron) in the vicinity of the nucleus. There are two characteristic features of photoionization cross-sections. First, the cross-sections do not simply decrease monotonically with increasing photon energy above the ionization threshold but in fact exhibit delayed maxima which depend on the *l* value of the orbital from which the electron is ejected [31–33]. As the *l* value of the orbital increases, the delayed maximum in photoelectron intensity shifts to higher energy above threshold and its magnitude decreases. This is caused by the repulsive centrifugal potential in the radial Schrödinger equation, which depends on l' ($= l + 1$) for the continuum state. This tends to keep the radial part of the continuum wavefunction very small in the vicinity of the initial orbital wavefunction, resulting in limited overlap and thus low photoelectron intensity. As E_k of the photoelectron increases, the continuum wavefunction penetrates this centrifugal barrier resulting in better overlap with the initial orbital wavefunction and thus greater intensity. The photon energy dependence of the photoionization cross-section of Cu 3d and Cl 3p orbitals are given in Fig. 9 [34]. The magnitude of the Cl 3p ($l = 1$) photoionization cross-section is high near the threshold, while that of Cu 3d ($l = 2$) has a delayed maximum of lower magnitude at ∼50 eV above threshold.

A second important feature is illustrated in the photoionization cross-section of Cl 3p in Fig. 9. The intensity drops rapidly to a value close to zero at ∼50 eV and then increases with higher photon energies. This is known as a Cooper minimum [31] and is due to the node in the 3p radial wavefunction. This minimum is present in the photoionization cross-sections of all orbitals which contain radial nodes (number of radial nodes = $n - l - 1$). As E_k of the electron increases, its wavelength decreases and thus its overlap

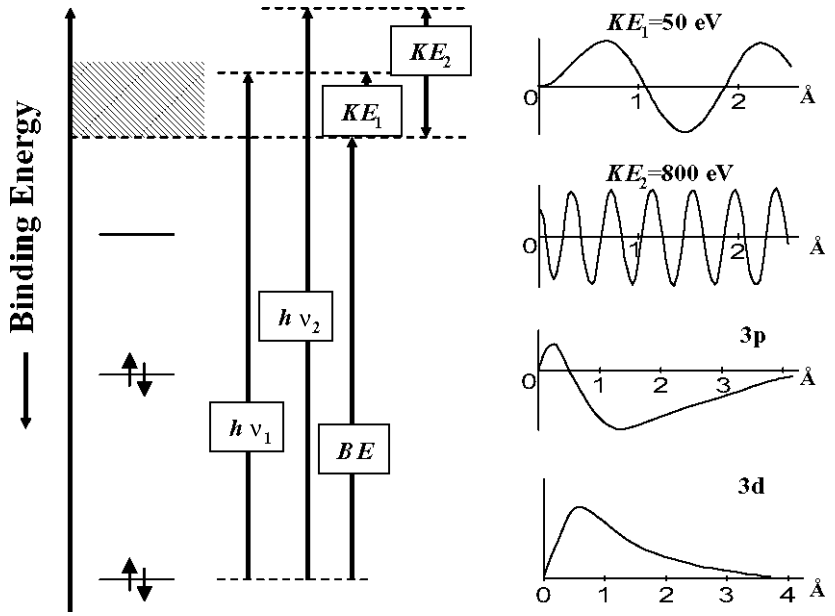

Fig. 8. Photon energy dependence of the photoionization cross-sections: Intensity of photoelectron peak varies depending upon input photon energy, due to the variation in the deBroglie wavelength of the outgoing photoelectron. These wavelengths are compared to the radial wavefunctions of Cu 3d and Cl 3p orbitals (right).

with the Φ_i changes. For Cl 3p at ~50 eV the overlap of the continuum radial wavefunction with the 3p orbital (Fig. 8) is such that there is effective cancellation of contributions of opposite sign to the electric dipole transition moment expression in Eq. (3.2). With further increases in $h\nu$ the wavelength of the radial wavefunction of the electron decreases and cancellation no longer occurs. For orbitals without radial nodes, the integral cannot change sign and thus will not exhibit this effect.

The variable-photon-energy photoelectron spectra of the valence level region of $Cu(I)Cl_4^{3-}$ in CuCl is shown in Fig. 10, left, which illustrate the photon energy dependent nature of the photoionization cross-sections [35]. Two main peaks are observed, separated by 3.5 eV. The peak at ~6 eV binding energy has the highest intensity at $h\nu = 26$ eV and decreases in intensity relative to the peak at binding energy of ~2.5 eV, reaching a minimum in the $h\nu = 45$ eV spectrum and then increasing slowly with higher photon energies. This is just the behavior predicted from the photoionization cross-sections for Cu 3d and Cl 3p given in Fig. 9 and allows a definitive assignment as indicated in Fig. 10.

The variable-photon-energy photoelectron spectra of $Cu(II)Cl_4^{2-}$ are shown in Fig. 10, right [35], and demonstrate that covalency can be determined from the photon energy dependence of PES peak intensities. The reduced energy difference between the Cl^- 3p and Cu(II) 3d valence levels leads to overlapping bands and more mixing of levels. The intensity dependence with variation in photo energy, however, clearly enables peak assignments. The peak to deeper binding energy starts relatively intense, reach a minimum at ~50 eV and increases again to higher photon

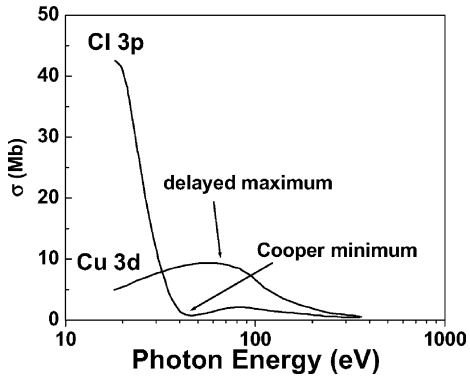

Fig. 9. Photon energy dependence of atomic photoionization cross-sections of Cu 3d and Cl 3p orbitals (adapted from reference [34]).

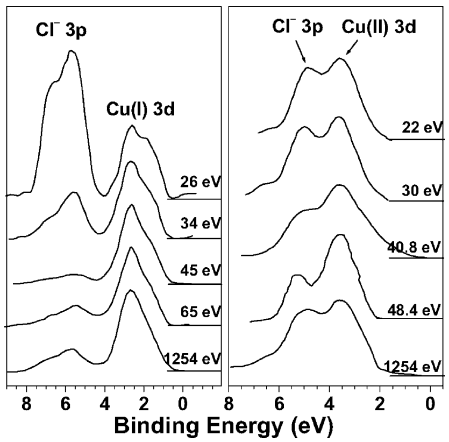

Fig. 10. Variable photon energy photoelectron spectra of the valence level region of T_d-$Cu(I)Cl_4^{3-}$ in CuCl (left) and D_{2d}-$Cu(II)Cl_4^{2-}$ in Cs_2CuCl_4 (right) (adapted from reference [35]).

Resonance: $3p^63d^{10} \xrightarrow{\text{Abs}} 3p^53d^{10}4s^1 \xrightarrow[\text{Auger}]{\text{SCK}} 3p^63d^84s^1$

Main PES: $3p^63d^{10} \longrightarrow 3p^63d^9$

Satellite PES: $3p^63d^{10} \longrightarrow 3p^63d^84s^1$

Scheme 2.

energy. It can therefore assigned as Cl^- 3p ionization; the lower binding energy peak again being from Cu 3d photoionization. There is, however, an important difference between Cu(II) and Cu(I) chlorides which is clearly demonstrated by the Cl^- 3p Cooper minimum data at ~50 eV. For $Cu(II)Cl_4^{2-}$, there is still a substantial amount of intensity in the Cl^- 3p peak. At this photon energy, this intensity must be due to Cu 3d photoionization which clearly requires that there be a significant amount of mixing of Cu 3d character into the Cl band. Hence, this intensity is a direct experimental probe of covalency. These covalently mixed photoionization cross-sections can be quantitatively analyzed in correlation to the atomic cross-sections (Fig. 9) through the Gelius–Siegbahn model (see Section 4.2) [36,37].

3.2.3. Resonance effects

An additional important feature involving the photon energy dependence of peak intensity is the resonance interaction with a transition to a bound state. For Cu complexes, changes in valence level PES peak intensity are observed at the metal 3p absorption edge (the M edge). The PES resonance mechanism has been defined by Davis and is given in Scheme 2 for a d^{10} (i.e. Cu(I)) complex [38].

At photon energies corresponding to the 3p → 4s absorption edge, a metal 3p electron is excited to the metal 4s orbital. This intermediate excited state then decays via an Auger process whereby a 3d electron fills the 3p hole and a second 3d electron is ejected. This Auger process involves a Super–Coster–Kronig transition (SCK) in which both the initial and final state holes reside in the same principal quantum shell ($n = 3$) [39]. The SCK transition has a high probability due to the localized nature and large repulsion of d electrons. The final state of this absorption plus Auger decay process is the same as that of the valence level satellite peak of a d^{10} complex (Scheme 2), which corresponds to a direct 3d photo-ionization plus a 3d → 4s shake-up transition. Thus, the resonance and satellite channels both involve the same final state at the metal 3d → 4s absorption edge and lead to the resonance enhancement of the satellite peak intensity. The valence resonance PES spectra of d^{10} CuCl are shown in Fig. 11, left [35]. As the photon energy is scanned through the Cu 3p absorption edge (~77 eV), the satellite intensity is greatly enhanced. The resonance effect is most clear in the constant initial state (CIS) experiment, where both the photon energy and the electron kinetic energy are scanned while keeping the binding energy fixed so that the intensity profile of a specific PES peak (in this case,

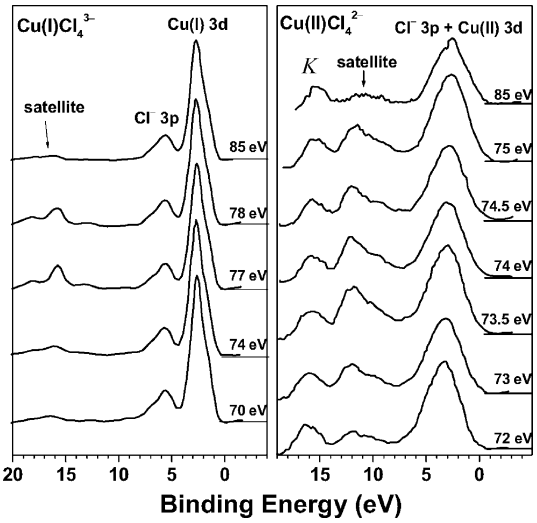

Fig. 11. Resonance photoemission spectra of $Cu(I)Cl_4^{3-}$ in CuCl (left) and $Cu(II)Cl_4^{2-}$ in $KCuCl_3$ (right) at the Cu 3p absorption edge (adapted from reference [35]).

the satellite peak) can be determined. The CIS intensity profile of the CuCl satellite peak clearly shows the resonance enhancement at the Cu 3p → 4s absorption edge (Fig. 12, left) [35]. The latter is observed from the constant final state (CFS) spectrum [40] also included in Fig. 12, left. This is basically an absorption experiment which in this energy region directly probes the Cu 3p → 4s transition, in correlation to the CIS intensity profile.

PES satellite peak non-resonance intensity in the valence level is also due to final state relaxation. Several spectral features of $Cu(II)Cl_4^{2-}$ in Fig. 11, right, show that large relaxation effects occur for this system and allow quantitation of these effects [35]. The peak at ~8 eV deeper binding energy relative to the composite valence peaks at 3–5 eV is a satellite band, which in an initial state model corresponds to ionization of an electron from the ligand orbital and simultaneous shake-up of a second ligand electron into the metal 3d

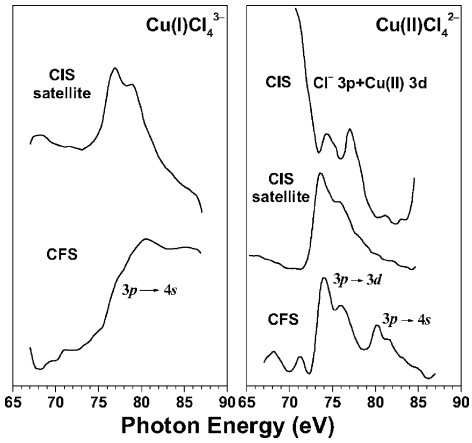

Fig. 12. Constant initial state (CIS) intensity profiles and the constant final state (CFS) spectra of $Cu(I)Cl_4^{3-}$ in CuCl (left) and of $Cu(II)Cl_4^{2-}$ in $KCuCl_3$ (right) (adapted from reference [35]).

Resonance: $3p^63d^9 \longrightarrow 3p^53d^{10} \xrightarrow{\text{Auger}} 3p^63d^8$

Main PES (Initial State Model): $3p^63d^9 \longrightarrow 3p^63d^8$

Satellite PES (Initial State Model): $3p^63d^9 \longrightarrow 3p^63d^{10}\underline{L}^2$

Scheme 3.

hole (Scheme 3, where $\underline{L}$, ligand hole). Since this is formally a two-electron process, the fact that it has non-resonance intensity requires that final state relaxation has occurred.

The extent of the relaxation process can be elucidated through the intensity behavior of the satellite with input photon energy between 72 and 85 eV photon energy. The satellite peak dramatically increases in intensity, maximizes at ~73.5 eV and then decreases with higher input photon energy (Fig. 11, right). The CIS profile of this peak is plotted in Fig. 12, right, along with the CIS profile of the Cu 3d and Cl 3p valence band peaks. The CFS spectrum shows the Cu 3p → 3d and 4s absorption edges. Thus, the satellite is exhibiting a resonance effect at the Cu 3p → 3d absorption edge.

Excitation at the Cu 3p absorption edge produces a $3p^53d^{10}$ excited state, which is able to undergo a very efficient Auger decay process (SCK decay) resulting in a $3p^63d^8$ final state (Scheme 3). This is also the state reached by direct ionization of the metal 3d level, which should be resonance enhanced. The key point here is that the dominant resonance is in fact occurring in the satellite peak (Fig. 12, right). As shown in Scheme 3, the satellite formally corresponds to two holes on the ligand yet the intensity involves a two hole metal (i.e. a $3d^8$) final state (initial state, $3d^9$, one hole in the metal ion). Therefore, extensive relaxation has occurred on metal ionization. This is due to the change in valence electron–electron repulsion which is ~6.5 eV for copper chlorides and can have dominant effects on final states, the nature of which can be defined by resonance PES as described above. Relaxation effects can thus be quantitatively studied by the PES experiment and correlated to density functional calculations, which are discussed below.

4. Electronic structure and electronic relaxation from PES

PES provides a unique perspective into the electronic structure of transition metal complexes. However, the perturbation caused by the ionization process provides several challenges for the interpretation of PES data. It is often assumed that the PES spectrum directly reflects the electronic (i.e. molecular orbital) structure of the molecular ground state by invoking Koopmans' theorem, which effectively states that the electronic structure of the ionized state is well-approximated by the electronic structure of the initial (non-ionized) molecule. Others have concluded that PES reflects the final (oxidized) state of the molecule and yields very little information about the initial (reduced) molecule. Reality, however, falls between these two extremes and PES data provide insights into the electronic structures of both the initial and final states of the system.

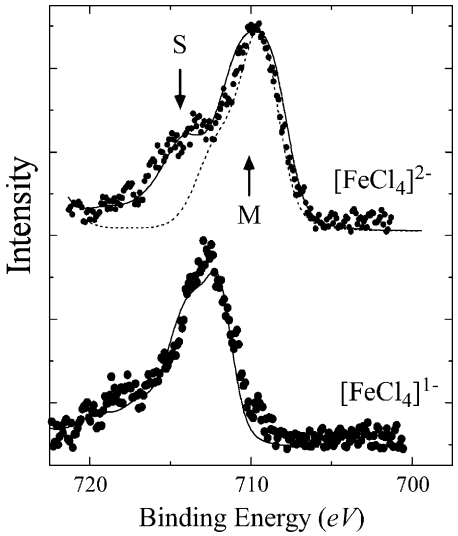

Fig. 13. Fe $2p_{3/2}$ core ionization data for $[N(CH_2CH_3)_4]_2[Fe(II)Cl_4]$ and $[N(CH_2CH_3)_4][Fe(III)Cl_4]$. Simulations including atomic multiplets (dashed line) and atomic multiplets with charge transfer states (solid lines) are superimposed on the experimental data points in each case [41].

The ability to extract both initial and final state information from PES data is particularly interesting for systems where redox processes are chemically meaningful. For redox-active species, PES is a direct probe of oxidation processes and can thus be used to evaluate the effect of electronic structure on redox processes directly. It further allows experimentalists to evaluate changes in electronic structure that occur as a result of redox events, i.e. PES is a direct probe of electronic relaxation upon ionization.

The ferrous and ferric tetrachloride redox couple has been chosen as an illustrative example of the methods that are available to evaluate both electronic structure and electronic relaxation. The details of the available experimental data are first presented and then evaluated using density functional (DFT) methods. A method for evaluating electronic relaxation directly from the experimental data is also developed using a valence bond configuration interaction (VBCI) model, which is compared to results obtained from DFT methods.

4.1. Experimental interpretation of PES data for iron tetrachloride

4.1.1. Core level Fe $2p_{3/2}$ PES data

Fe $2p_{3/2}$ core ionization data for $[N(Et)_4][Fe(III)Cl_4]$ and $[N(Et)_4]_2[Fe(II)Cl_4]$ are shown in Fig. 13 [41]. The ferric species yields a single $2p_{3/2}$ ionization peak with some additional intensity at higher binding energies causing asymmetry in the band shape. Even though this core ionization process (Fe $2p_{3/2} \rightarrow \infty$) is quite simple, there are many possible $2p^53d^5$ final states due to the atomic multiplet structure of the transition metal ion. This multiplet

structure distributes intensity over a large number of final states and is at least partially responsible for the observed asymmetry at higher binding energies. Theoretical simulations of atomic multiplet structure for ionization, corrected for the symmetry of the surrounding ligand field and for nephelauxetic decreases in calculated ionic Slater integrals, can be used to provide good agreement with the observed ferric core ionization data.

The core ionization data for the ferrous complex are strikingly different from that which is observed for the related ferric species. In this case, the data show a strong second ionization peak at deeper binding energy that cannot be simply described by the atomic multiplet structure of the $2p^5 3d^6$ final states (dashed line in Fig. 13 gives the calculated multiplet shape of $2p_{3/2}$ ionization). It has been recognized that these additional features in a core ionization spectrum result due to contributions from additional final states—specifically from "shake-up" transitions that involve transfer of lower energy ligand-based electrons into the metal 3d manifold, yielding $2p^5 3d^7\underline{L}$ final states (where $\underline{L}$ represents a hole in the ligand orbitals). These shake-up satellite peaks are a spectroscopic manifestation of electronic relaxation; these transitions are formally forbidden two electron processes and can only have intensity if the electronic wavefunction changes as a result of the ionization process. A valence-bond configuration interaction (VBCI) model that allows for these additional charge transfer (CT) final states can be introduced as a perturbation to the atomic multiplet structure, which significantly improves the correlation between the multiplet simulations for the ferrous species and the experimental data. The details of this VBCI model are provided below (Section 4.3).

4.1.2. Valence PES data

The valence region is significantly more complex due to the greater number of possible ionization processes; all atoms within a sample will contribute in this region. The loss of atom-specificity in the valence region can in part be overcome by exploiting the orbital-specific behavior of atomic orbital cross-sections as described in Section 3.2.2, thus allowing peak assignments. The variable photon energy valence PES data for both $Cs[Fe(III)Cl_4]$ and $Cs_2[Fe(II)Cl_4]$ are shown in Figs. 14 and 15, respectively [42,43]; in each case, the intensity of the valence photoionization peaks is strongly dependent on the energy of the incident photons. The characteristic "delayed maximum" of *n*d-type atomic orbitals at ~50 eV can be used to qualitatively evaluate which ionization peaks correspond with predominantly Fe 3d ionization and therefore Fe 3d-based molecular orbitals. The Cl 3p provides a complementary cross-section, having a Cooper Minimum due to the node in the 3p radial wavefunction at ~50 eV.

For the ferrous species (Fig. 15), the lowest binding energy peak (labeled RAMO, the redox active molecular orbital) is well separated from a manifold of three overlapping peaks (labeled A, B, C). At even deeper energies, other

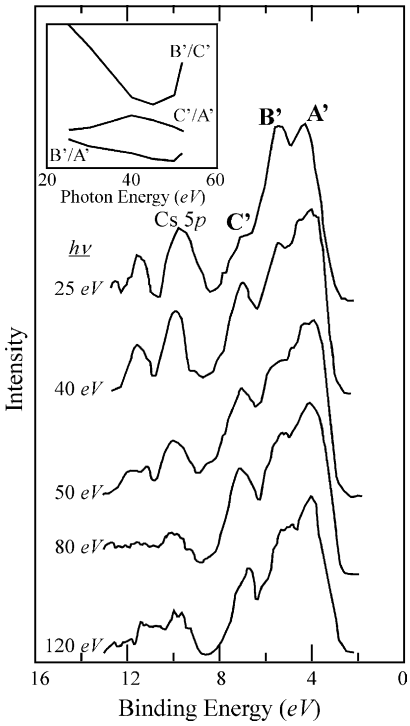

Fig. 14. Variable photon energy PES (VEPES) data for $Cs[Fe(III)Cl_4]$. The inset shows the relative photoionization cross sections for each of the peaks in the spectra. From these cross sections, metal character is localized mostly in peak C′ and to a less extent in peak B′—at deep binding energies. Data and analysis from reference [43].

peaks including satellites (labeled S) also appear. From the cross-section behavior of these peaks (see inset, Fig. 15) we observe that the two lowest-binding energy peaks (RAMO, A) clearly contain significant 3d character whereas the deeper binding-energy region (B, C) contains greater ligand character. (See A/B ratio Fig. 15 inset (dashed line) which shows delayed maximum in A relative to peak B). The higher energy (i.e. lower binding energy) of the filled metal-based valence orbitals is in keeping with traditional ideas of bonding in transition metal systems, where the metal 3d orbitals are above the ligand valence orbitals. A superficial comparison of these data with those of the ferric species (Fig. 14) seems to indicate that the one-electron oxidized site is very similar to the ferrous site, except for the absence of the RAMO peak, the lowest binding-energy peak. From this, one can qualitatively infer that this peak corresponds with ionization of the extra spin-down electron in the high-spin Fe $3d^6$ manifold to generate the $S = 5/2$ Fe $3d^5$ species in the final state. Without the benefit of variable photon-energy data, it would seem reasonable to suggest that the electronic structure of the ferrous and ferric sites are very similar, differing only in the presence of the low energy additional electron peak in the $3d^6$ system. The variable photon energy data for the ferric species (see inset, Fig. 14) indicate a far more complex (and interesting) behavior. Peak A′ does not behave in a manner that is consistent with metal 3d character. The lowest binding-energy

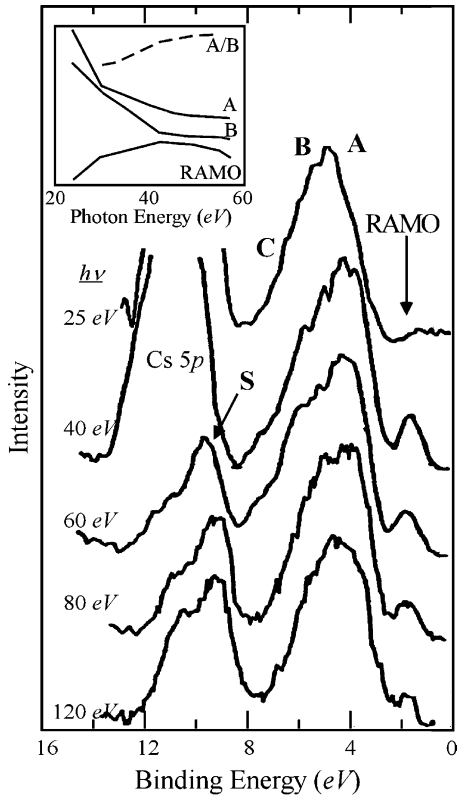

Fig. 15. VEPES data for $Cs_2[Fe(II)Cl_4]$. The inset shows the cross-section behavior of the main peaks in the spectrum; the metal character is localized mostly in the low binding-energy region (RAMO and A) rather than at deeper binding energy. Data and analysis are given in reference [42].

region (A′) in fact carries mostly ligand character, whereas the metal 3d character has shifted to region C′ at much deeper binding energy. (C′/A′) in Fig. 14 inset shows a positive delayed maximum). This dissimilarity reflects a dramatically different electronic structure in the Fe(III) system as compared to the Fe(II) even though they only differ by the presence of a single electron.

In the ferrous case, the cross section behavior demonstrates that the highest-lying orbitals contain predominantly metal character, as it should when applying the normal molecular orbital description of transition metal complexes. As shown in Fig. 16, the valence Fe 3d orbitals should

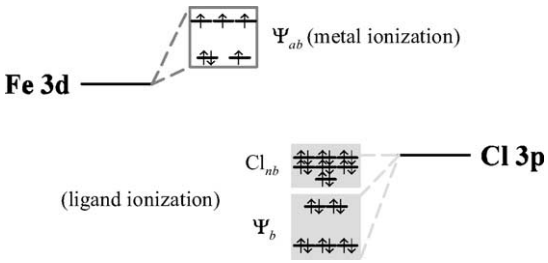

Fig. 16. Normal molecular orbital representation of first row transition metal complexes. The highest-lying filled orbitals have predominantly metal character and thus should correspond to metal ionization peaks in the PES spectrum.

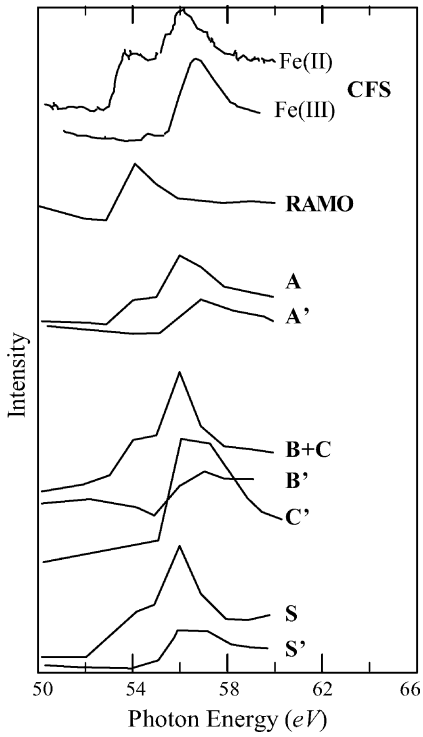

Fig. 17. Resonance behavior of valence PES data for ferrous (above) and ferric (below) complexes. The labeling corresponds with that given in Figs. 14 and 15.

interact with the deeper energy valence Cl 3p orbitals (due to its greater electronegativity) to form a set of predominantly Cl 3p-based bonding molecular orbitals (e and t_2 in T_d symmetry), with a complementary set of higher-energy Fe 3d-based antibonding orbitals (e* and t_2^*). A set of purely non-bonding Cl 3p orbitals should also be present at energies between the ligand bonding and metal bonding orbitals. This "normal" transition metal bonding scheme is perfectly adequate to describe the observed behavior for $[FeCl_4]^{2-}$.

According to the MO representation given in Fig. 16, it would seem reasonable to expect only small differences between the ferrous and ferric species. The analysis of the $[FeCl_4]^{1-}$ PES data however, suggest that its highest energy orbitals have mostly Cl 3p character and that the Fe 3d orbitals are much lower in energy. This inversion of the predicted molecular orbital ordering in the ferric species indicates the failure of the model and the need for an "inverted bonding scheme" to describe the ferric PES data [43]. The electronic origin of this inverted bonding description is addressed in detail in Section 4.2 using electronic structure calculations.

The differences in the observed behavior between the ferrous and ferric species further extends to their resonance behavior of the valence PES data at the Fe 3p ionization edge (~52–56 eV) as shown in Fig. 17. As described in Section 3.2.3, resonance enhancement provides a direct probe of final state effects for a particular ionization pro-

cess. In the ferric species, Fe 3p-based resonance enhancement is observed in the energy region of peak C′ as well as in deeper binding energy satellites (near the Cs peaks at ∼12 eV. See reference [44]) that generally have only weak intensity out of resonance. Qualitatively, this is interpreted as resulting from only small changes in the electronic structure upon valence ionization of the Fe $3d^5$ species to the Fe $3d^4$ final state. The weak off-resonance intensity of the satellite features, as well as the correspondence between the metal 3d contributions to the initial state and in the final states between non-resonance and resonance cross-sections provide direct experimental evidence that electronic relaxation is quite small for valence ionization of the ferric species. The weak contributions from shake-up satellites in the Fe $2p_{3/2}$ ionization data (Fig. 17) further support the description that the electronic structure of the ferric species is robust to ionization. The ferric species thus has an unusual inverted orbital scheme, which remains unchanged on oxidation.

The ferrous species behaves very differently. The metal-based RAMO and A ionization peaks are only slightly enhanced over the Fe 3p edge, whereas the ligand-based ionizations in region C show dramatic resonance enhancement. Importantly, the resonance enhancement profile parallels the behavior of peak C′ in the ferric species, which is also resonance enhanced. From this, we conclude that the metal character shifts to deeper binding energy on ionization of the ferrous species. This is confirmed by the intense satellite features at deeper binding energy (∼10 eV), which are quite prominent even out of resonance (Fig. 15, $h\nu = 60$ eV, peak S). Therefore, the $3d^6 \rightarrow 3d^5$ ionization process is accompanied by a significant rearrangement of the molecular orbital structure that shifts metal character to deeper binding energy. Again, the core-level ionization behavior corresponds nicely with the valence behavior—in this case, the large intensity of the shake-up satellite (see Fig. 13) confirms that the electronic structure of the Fe $3d^6$ state changes significantly upon oxidation. As clearly demonstrated by the experimental data, the electronic structure of $[FeCl_4]$ changes from a normal bonding scheme in ferrous to the inverted scheme experimentally observed for the ferric species.

This section has been limited to the analysis of PES data based solely upon the qualitative interpretation of the available variable photon energy data. This approach is extremely powerful and much insight can be derived from such analysis. In this case, the experimental core and valence data provide a qualitative bonding picture that differs substantially between the Fe(II) and Fe(III) tetrachloride complexes. The data also indicate that the final states for Fe(II) ionization are consistent with the electronic structure picture obtained for the Fe(III) species. At this point, it is extremely useful to quantitate the analysis and utilize available theoretical tools to provide additional detail and further insights into the observed spectroscopic behavior.

4.2. Electronic structure calculations

The simplest model for correlating PES spectra with electronic structure calculations to apply Koopmans' theorem; the spectrum is assumed to reflect the molecular orbital description of the initial (reduced) ground state. From this, it is possible to simulate PES spectra from ground state electronic structure descriptions provided by density functional theory (DFT) calculations on transition metal sites of interest. Peak energies are obtained from the molecular orbital energy splittings, although these must generally be corrected for spin and orbital multiplet effects not explicitly included in the single-determinant DFT molecular orbitals. Peak intensities are calculated using the Gelius–Siegbahn model, which treats that the ionization probability of an electron in a particular molecular orbital Ψ_k (I_k) as a weighted sum of the ionization probabilities of its component atomic orbitals (σ_j).

This assumption is appropriate if the incident photon energy is large (>150 eV) such that the outgoing photoelectron couples poorly with the final state or if one atomic orbital cross-section dominates thus minimizing cross-terms between different orbital contributions. In first row transition metal complexes, this is always satisfied for core ionizations and can be obtained in valence PES experiments by using the characteristic photoionization cross-section behavior of the component atomic orbitals to maximize contributions from specific atomic orbitals. For example, the delayed maximum in metal 3d orbital cross-sections yields a maximum at relatively high photon energies (∼40–50 eV) where other cross-sections (s- and p-type atomic orbitals) are very weak. For $[FeCl_4]^{2-/1-}$, the combined effect of the Fe 3d delayed maximum and the Cl 3p Cooper minimum at similar energies provides a good system for application of the Gelius–Siegbahn approach to simulate valence PES data.

Several density functionals are currently utilized with varying success depending on the nature of the systems being studied. On the whole, no particular functionals have emerged as the most reliable for transition metal systems, especially within the context of simulating photoelectron and other spectroscopic data. It is generally advisable to include generalized gradient correction terms for both exchange and correlation to supplement local density approximations. Notably, hybrid functionals such as B3LYP (which contain some Hartree Fock exchange, which tends to lower the covalency) have become particularly popular in recent years. A most effective approach is to test several functionals and hybrids with respect to their ability to adequately simulate known spectroscopic data for the systems of interest. For example, we have found that the UV-Vis electronic spectra for $[FeX_4]$ complexes are well simulated by VWN-BP86 calculations using a triple-ζ Slater basis set. These calculations still somewhat overestimate π contributions to bonding, which must be taken into account during any subsequent analysis of the computational results.

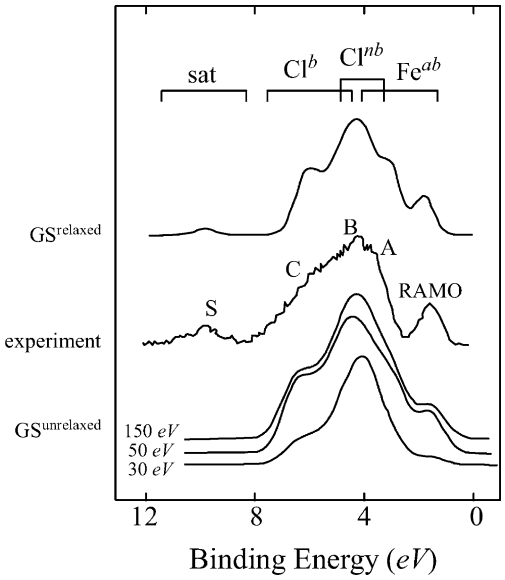

Fig. 18. PES simulations obtained by applying the Gelius–Siegbahn model to initial state unrelaxed DFT wavefunctions (bottom, $GS^{unrelaxed}$) compared to the experimental PES spectrum for Rb_2FeCl_4 at $h\nu = 50$ eV (middle), which has been labeled as in Fig. 15. A simulation of the same PES spectrum at $h\nu = 50$ eV is also shown using relaxed final state wavefunctions from DFT calculations as described in the text (top, $GS^{relaxed}$). The dominant contributions to each region of the ionization spectra are given above the spectra. See reference [42] for details.

Ground state spin-unrestricted DFT calculations of $[FeCl_4]^{2-}$ have been used to quantitatively simulate the variable photon energy PES spectra (Fig. 18, bottom), yielding good overall agreement with the experimental data. The lowest binding energy peak corresponds to the ionization of the single minority spin 3d electron; its photon energy dependence shows a delayed maximum (as evidenced by a large increase in intensity from 30 to 50 eV) that strongly mimics that which is seen for the RAMO peak in the experimental spectrum (as shown in Fig. 15, inset). At deeper binding energy, the majority spin Fe 3d electrons and the valence Cl 3p electrons both contribute to a broad envelope of peaks that correspond to peaks A, B, and C in the experimental spectrum. The theoretical spectrum indicates that the lower binding energy peak A contains greater metal character, whereas the deeper binding energy peaks B and C contain mostly ligand character. Importantly, the unrelaxed theoretical spectra obtained from the Gelius–Siegbahn approach ($GS^{unrelaxed}$) do not show any intensity at deeper binding energies and thus cannot account for peak S in the experimental spectrum. The problem is that relaxation of the electronic structure is not allowed to occur within the context of Koopmans' theorem, resulting in the lack of shake-up satellite peaks in the theoretical spectrum.

A modification of the Gelius–Siegbahn approach is to use relaxed ionized final state wavefunctions to obtain both the energies and intensities of the ionization peaks (Fig. 18, $GS^{relaxed}$). The distribution of intensity over these final states is obtained by projecting the initial state terms onto the component final states using the sudden approximation [21]. The frozen orbital final states can be expanded in terms of the relaxed final states of the ion ($\Psi_R(N-1) = \Sigma_i(\Psi_i|\Psi_R > \Psi_i(N-1)$), where $\Psi_R(N-1)$ is the remainder wave function of the frozen orbital after one-electron ionization, and $\Psi_i(N-1)$ are the ground and excited states of the relaxed ion. The total intensity for the $\Psi_R(N-1)$ frozen orbital state is thus partitioned among all the possible final states of the relaxed ion. Using this relaxed final state approach, the variable photon energy PES simulations (Fig. 18) result in additional intensity at deeper binding energy, accounting for the intense experimentally observed satellite features (S) that result primarily from LMCT excitation in addition to ionization (i.e. 2-electron transitions).

Importantly, the qualitative insights from the experimental data are well reproduced by proper analysis of ground and excited state wavefunctions from DFT calculations including electronic relaxation. The agreement provides increased confidence in the ground state description obtained from DFT methods and allows for a more quantitative investigation of the electronic structure of such complexes. At this juncture, we can revisit the bonding description of the $[FeCl_4]^{2-,1-}$ redox couple to obtain further insight into the inverted bonding description that clearly exists in the ferric species. Fig. 19 shows qualitative MO representations of $[FeCl_4]^{2-,1-}$ obtained from spin-unrestricted DFT calculations supported by the VEPES data. These calculations use two sets of MOs to describe the majority (spin-up) and minority (spin-down) orbitals, an approach that allows for spin polarization of the electronic structure due to the high spin state of these complexes. As expected, the electronic structure of the ferrous species is quite "normal"—the Fe 3d-based orbitals (spin-up and spin-down) are higher in energy than the Cl 3p-based orbitals. The electronic

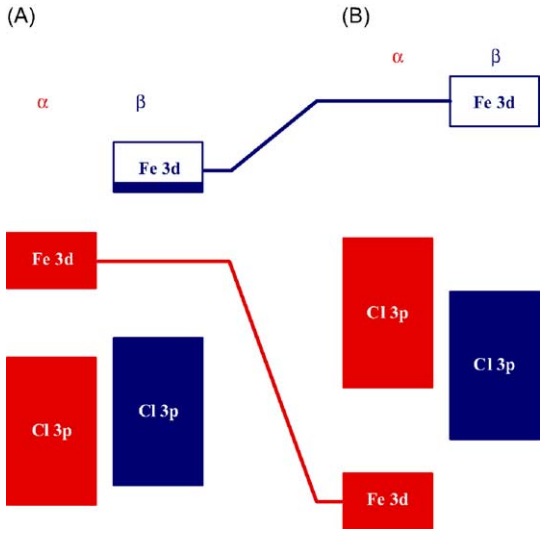

Fig. 19. Qualitative spin-unrestricted molecular orbital representations of (A) $[FeCl_4]^{2-}$ and (B) $[FeCl_4]^{1-}$. The shaded regions represent filled molecular orbitals whereas unshaded regions are empty.

structure of the ferric species is quite different. The high spin S = 5/2 state of this $3d^5$ system causes a significant increase in the spin polarization (splitting between the spin-up and spin-down orbitals), which stabilizes the filled spin-up Fe 3d orbitals below the Cl 3p manifold. The highest lying filled orbitals now mostly contain Cl 3p character, leading to the experimentally observed inverted bonding scheme.

A similar analysis of core ionization behavior using the Gelius–Siegbahn approach is possible in theory, but time-independent DFT methods yield rather poor descriptions of the core hole resulting from ionization. An alternative approach is the use of valence bond states to construct many-electron initial and final states through configuration interaction. The correlation of these states to the simpler molecular orbital picture is more complex but it allows a direct correlation between the initial and final states of the PES experiment and thus the explicit evaluation of changes to the molecular wavefunction on ionization.

4.3. Valence bond configuration interaction

It is simplest to consider the influence of electronic relaxation within the context of the limiting valence bond states, i.e. purely ionic component configurations that are allowed to mix through configuration interaction. Such an approach is known as a valence bond configuration interaction (VBCI) model, and it is developed in detail for core ionization and the analysis of core PES data. The approach can be extended to valence PES data if atomic multiplet effects are explicitly evaluated.

4.3.1. Two state VBCI model for core ionization

A representation of the VBCI model for core ionization is given in Fig. 20; the electronic structure of the initial state is represented by configurational mixing between the ground $|d^n\rangle$ configuration and a higher energy ligand-to-metal charge transfer (LMCT) configuration $|d^{n+1}\underline{L}\rangle$, where $\underline{L}$ represents a valence hole in the ligand orbitals. The resultant ground VBCI states (Ψ_i^M and Ψ_i^L) are defined by the matrix shown in Eq. (4.1a). The parameters T and Δ represent the interaction (or covalent mixing) parameter (proportional to ligand–metal overlap) and the splitting of the unmixed metal and LMCT configurations, respectively. The ground state covalency is determined by $\alpha_i^2 = \cos^2\theta_i$, which designates the metal character in the wave function where θ_i is defined from Eq. (4.1b). The energy of the LMCT transition ($W_i = E_{CT}$) is also obtained from this treatment as given in Eq. (4.1c). The VBCI approach assumes that overlap between the initial $|d^n\rangle$ and $|d^{n+1}\underline{L}\rangle$ configurations is induced by the off-diagonal term, T.

$$\begin{bmatrix} 0 & T \\ T & \Delta \end{bmatrix} \quad \begin{aligned} \Psi_i^M &= \cos\theta_i\,|d^n\rangle - \sin\theta_i\,|d^{n+1}\underline{L}\rangle \\ \Psi_i^L &= \sin\theta_i\,|d^n\rangle + \cos\theta_i\,|d^{n+1}\underline{L}\rangle \end{aligned} \tag{4.1a}$$

$$\tan(2\theta_i) = \frac{2T}{\Delta} \tag{4.1b}$$

$$W_i = E_{CT} = \sqrt{\Delta^2 + 4T^2} \tag{4.1c}$$

The ionized final states (Ψ_f^M and Ψ_f^L) are defined in an analogous manner except that the relative energies of the metal-centered $|\underline{c}d^n\rangle$ and ligand-centered $|\underline{c}d^{n+1}\underline{L}\rangle$ configurations ($\underline{c}$ = core hole on metal) have changed due to the differential effect of the 2p − 3d hole interaction potential (Q) on each configuration. The core hole destabilizes the $|\underline{c}d^n\rangle$ configuration by an amount Q relative to $|\underline{c}d^{n+1}\underline{L}\rangle$ since there is additional hole-hole repulsion in that configuration; the energy splitting between the two configurations is therefore $\Delta - Q$. In cases where $Q > \Delta$, the order of the two VB configurations inverts relative to that which is observed in the ground state. The VBCI final states and all associated final state parameters are defined as in Eq. (4.2) with the order of the final states defined by the sign of $(\Delta - Q)$. In this model, the core hole results in the addition of Q in the CI matrix, which changes the relative contributions of the two

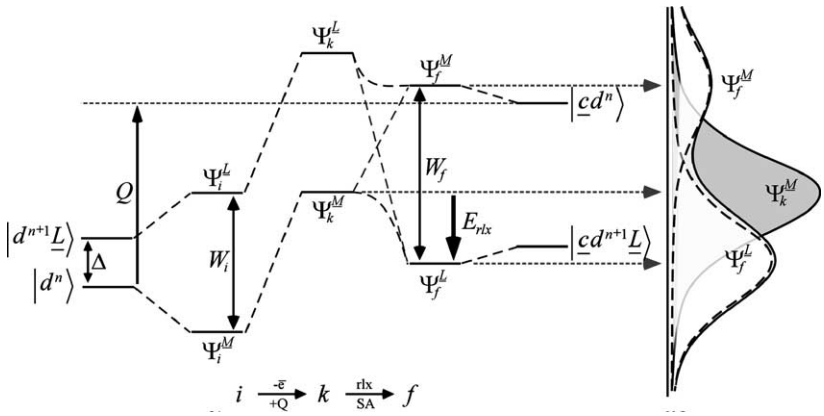

Fig. 20. Representation of a two-state valence bond configuration interaction (VBCI) model for analysis of core ionization processes. The observed intensity for the ionization transition distributes amongst the two relaxed final states to generate the lower-energy main peak and higher-energy satellite peak.

component states in the final state ($\alpha_f^2 = \sin^2\theta_f \neq \alpha_i^2$).

$$\begin{bmatrix} Q & T \\ T & \Delta \end{bmatrix} \begin{matrix} \Psi_f^M = \cos\theta_f \,|c\underline{d}^n\rangle - \sin\theta_f \,|c\underline{d}^{n+1}L\rangle \\ \Psi_f^L = \sin\theta_f \,|c\underline{d}^n\rangle + \cos\theta_f \,|c\underline{d}^{n+1}L\rangle \end{matrix} \quad (4.2a)$$

$$\tan(2\theta_f) = \frac{2T}{(\Delta - Q)} \quad (4.2b)$$

$$W_f = \sqrt{(\Delta - Q)^2 + 4T^2} \quad (4.2c)$$

For the wave functions chosen, a certain number of restrictions are needed to limit the solution set: for $\Delta > 0$ then $0^\circ < \theta_i < 45^\circ$, for $(\Delta - Q) > 0$ then $0^\circ < \theta_f < 45^\circ$, and for $(\Delta - Q) < 0$ then $45^\circ < \theta_f < 90^\circ$. Within this formalism, the $\Psi_i^M \rightarrow \Psi_f^M$ ionization is an allowed one-electron process whereas $\Psi_i^M \rightarrow \Psi_f^L$ is a formally forbidden two-electron transition known as a "shake-up transition" since a second electron is internally excited in addition to the metal-based core ionization. Intensity into the Ψ_f^L final state results from electronic relaxation (driven by Q), which reorganizes electron density and creates a situation where Ψ_f^L is not formally orthogonal to the Ψ_i^M ground state.

The degree of electronic relaxation is thus related to the intensity of the $\Psi_i^M \rightarrow \Psi_f^L$ transition, which can be described within the VBCI model by generating a reference ionized state where orthogonality between the initial and final state wave functions is enforced. This reference state, termed the Koopmans state results from core ionization without electronic relaxation. The description of the wave functions is frozen such that $\theta_k = \theta_i$ (and thus $\alpha_k^2 = \alpha_i^2$), but the energy of the Koopmans states are allowed to change based upon the amount of $|c\underline{d}^n\rangle$ character in each of the two wave functions. The energy destabilization due to Q thus distributes over the two-component Koopmans states as shown in Eq. (4.3).

$$\begin{aligned} E_k^M &= E_i^M + Q(\alpha_i^2) \\ E_k^L &= E_i^L + Q(1 - \alpha_i^2) \end{aligned} \quad (4.3)$$

From this construction, electronic relaxation is defined as the change between the ionized Ψ_k^M and Ψ_f^L (when $Q > \Delta$) wave functions. Changes in the wave functions due to electronic relaxation are quantified as the difference in the effective charge on the metal on going from the unrelaxed to the relaxed final states; this change in charge due to electronic relaxation (Δq_{rlx}) is calculated as given in Eq. (4.4) (specifically for $Q > \Delta$). The energetic effect of electronic relaxation (E_{rlx}) can also be calculated as the energy difference between the unrelaxed and relaxed final states.

$$\Delta q_{rlx} = \alpha_k^2 - \alpha_f^2 = \alpha_i^2 - \alpha_f^2 = \cos^2\theta_i - \sin^2\theta_f \quad (4.4)$$

Experimentally, the degree of electronic relaxation is reflected by the relative intensity of the forbidden shake-up transition relative to the main one-electron ionization peak (I_S/I_M). This intensity ratio can be used to determine the relationship between the Koopmans and true final states through Eq. (4.5), obtained from sudden approximation [21].

$$\frac{I_S}{I_M} = \tan^2(\theta_f - \theta_i) \quad (4.5)$$

The basic VBCI model presented above assumes that the ionization process is well-described by a single one-electron ionized final state and the presence of only one available LMCT state. In reality, neither of these assumptions is general. A multitude of possible metal-based final state configurations are possible (except for d^{10} final states) as determined by the atomic multiplets that result from the $|c\underline{d}^n\rangle$ configuration. In most cases, this serves to distribute intensity over a number of different final states that can all be perturbed by the presence of appropriate LMCT states. In fact, significant debate has occurred over the best description of satellite features in core PES spectra. Simulations that combine both atomic multiplet and charge transfer contributions, as developed by Thole and coworkers [45,46], provide the most effective method of evaluating these different contributions.

4.3.2. Core VBCI simulation of iron tetrachloride

The Fe $2p_{3/2}$ ionization of the $[FeCl_4]^{2-,1-}$ redox couple provides a useful illustration of the relative importance of atomic multiplets and charge transfer contributions to higher-energy satellite peaks. In the ferric species, there is significant asymmetry in the peak shape that is well described by an intensity distribution elucidated from final state atomic multiplets (see Fig. 13 bottom); charge transfer contributions to the spectrum are thus very small in this case. By contrast, the large satellite feature in ferrous tetrachloride (Fig. 13 top) cannot be completely simulated by atomic multiplet calculations of the core ionization process (dotted line); significant LMCT (and thus electronic relaxation) contributions to the ionization of the ferrous species must be included to adequately simulate the experimental spectrum (solid line).

The qualitative results for core ionization of $[FeCl_4]^{2-}$ are therefore very similar to that which has been obtained for valence ionization—the final ionized states differ substantially from the initial reduced states, indicating a large degree of electronic relaxation on ionization. From the VBCI analysis, however, the amount of relaxation can be quantified through Δq_{rlx}. From the simulations in Fig. 13 top, $\Delta q_{rlx} \sim 0.8$e, which demonstrates that the effect is extremely large for this system. For ionization of the ferric species, an upper limit of $\Delta q_{rlx} \sim 0.35$e is obtained.

4.3.3. Extension to valence ionization

The basic VBCI model shown in Fig. 18 can also be applied to valence ionization with a single modification: the 2p–3d hole interaction potential (Q) must be replaced by the 3d–3d hole interaction potential (U). An additional concern, however, is the applicability of the sudden approximation to calculate the intensity distribution over the final states, but

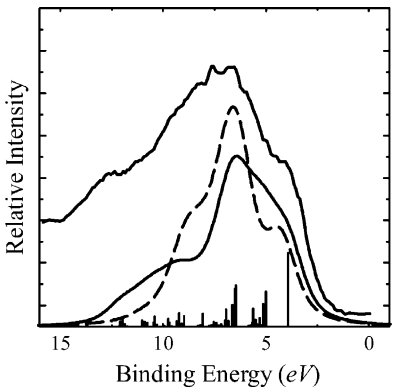

Fig. 21. AM + VBCI simulations of the valence PES spectrum (the normalized ratio of intensities at two photon energies, 45 and 25 eV, is used) for $[FeCl_4]^{2-}$ compared to the experimental spectrum. The dashed line is an AM simulation without electronic relaxation, whereas the solid line gives a complete AM + VBCI simulation (which includes electronic relaxation). Each component of the complete AM + VBCI simulation is also shown as a bar graph. Modified from reference [41].

it has been shown in several systems that the sudden approximation still provides good results even at lower photon energies.

However, the two state VBCI model above does not provide adequate simulations for valence ionization on its own since the spectrum will be dominated by atomic multiplet effects, which only play a limited role in the analysis of the core spectra for ferrous tetrachloride. The application of combined atomic multiplets AM and VBCI (AM + VBCI) methods is therefore necessary for adequate simulation of valence PES spectra. Fig. 21 shows the AM + VBCI simulations for $[FeCl_4]^{2-}$ both without and with electronic relaxation. As observed with the DFT-derived spectra for the same complex, the final state effects provide for significantly increased intensity at deeper binding energies due to the large influence of electronic relaxation. From these simulations, Δq_{rlx} can be calculated as was done for the core ionization process and is found to be ~0.7e, i.e. it is smaller than for core ionization but still extremely large, in agreement with both the qualitative experimental interpretation and the DFT-derived simulations.

5. Recent applications

In the last decade, photoemission spectroscopy has emerged as a powerful tool for studies of inorganic and bioinorganic systems. Synchrotron radiation with its continuous spectral distribution has opened up new directions for applications of photoelectron spectroscopy. Table 1 lists the recent PES studies on inorganic systems—small molecules and transition metal complexes. The effects and the applications of resonance, Cooper minimum and delayed maximum (cross-section effects) have been discussed in Sections 3 and 4. Jennifer C. Green's review in this volume focuses on the use of synchrotron radiation for PES experiments on organometallic and transition metal molecules. In this section, we will review two relatively new applications with selected examples. In Section 5.1.1 the focus is on the multi-atom resonance technique and Section 5.1.2 reviews the study of vibrational fine structures in the photoelectron spectra of small molecules. Section 5.2 focuses on Bioinorganic applications and provides an overview of the application of PES in evaluating electronic structure and electronic relaxation and defining their influence on the redox properties of important electron transport proteins.

5.1. Inorganic applications

5.1.1. Multi-atom resonant photoemission (MARPE)

Multi-atom resonance is observed when the incident photon energy is tuned to a core level absorption edge of an atom neighboring the emitting atom (inter-atomic resonance). Core photoemission peaks are enhanced when the emitting level has a lower binding energy than the resonant level. This was first studied by Fadley and co-workers [103–105] in the single crystals of inorganic transition metal compounds (MnO, Fe_2O_3 and $La_{0.7}Sr_{0.3}MnO_3$). The experiments were done at the Advanced Light Source, Berkeley, California.

The X-ray absorption spectrum of the Mn 2p region showing the $2p_{3/2}$ absorption at a binding energy of 639 eV and $2p_{1/2}$ absorption at 650 eV is shown in Fig. 22 bottom. The spectrum has been corrected (solid line) for non-linearity in the detector response. The O 1s PES spectrum with incident angle (θ_{hv}) at 10° and electron exit along the normal $\theta_{exit} = 90°$ was recorded from 630 to 660 eV. The total O 1s peak intensity is evaluated after subtracting the background of inelastic scattered electrons and the intensity variation as a function of photon energy is shown in Fig. 22 (top, excitation spectrum). The photoemission from the O 1s (binding energy of ~530 eV) level showed resonance (~12% in energy integrated intensity) at the $Mn2p_{3/2}$ and $2p_{1/2}$ absorptions (~639 and 650 eV). Similar resonance enhancements were observed in Fe_2O_3 (at the Fe 2p region ~705 eV) and in $La_{0.7}Sr_{0.3}MnO_3$ (Mn 2p). The observed resonances are

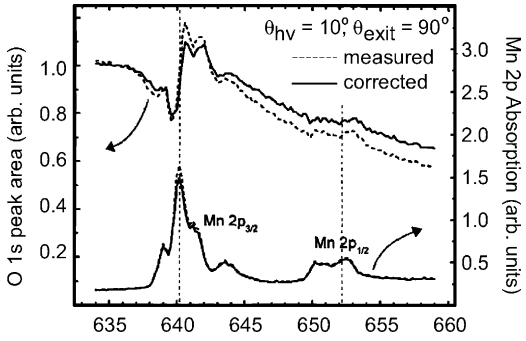

Fig. 22. MARPE effect in MnO. (A) O 1s photoemission peak intensities as a function of photon energy—excitation spectrum. (B) X-ray absorption coefficient for MnO. Data shown for $\theta_{hv} = 10°$ and $\theta_{exit} = 90°$ (dashed curve) (adapted from reference [103]).

Table 1
Recent PES studies using synchrotron radiation

Sample	Description of study	References
Transition metal complexes		
$Fe(CO)_5$	Valence band PES	[47]
$CeRuSi_2$	High resolution Ce 4d–4f resonance PES	[48]
$MnCl_2$, $CrCl_2$, VCl_2	Multi-atom resonance photoemission effects	[49]
Fe_3O_4	Spin resolved PES study	[50]
M(eta(3)-$C_3H_5)_2$, M = Ni, Pd, Pt	Photoionization cross-sections, VEPES	[51]
$CpM(CO)_2$, M = Co, Rh, Ir	VEPES: molecular orbital assignment	[52]
$M(CO)_5X$, M = Re, Mn; X = Cl, Br	High-resolution valence band VEPES	[53]
$W(CO)_6$, $W(CO)_5PMe_3$	Study of ligand field effects, ligand additivity effects	[54]
(eta(5)-C_5H_5)NiNO	Valence VEPES, resonance effects	[55]
M = Ni, Pd, Pt		
(eta(5)-C_5H_5)M(eta(3)-C_3H_5)	Valence VEPES, resonance effects	[56]
$Os(CO)_4L$, L = CO, PMe_3	High resolution VEPES, resonance, Cooper minimum effects	[57]
$CpM(CO)_3$, M = Mn, Re, Cr	Valence and core level PES	[53]
$CpFe(CO)_2I$	Core, valence and inner valence PES	[58]
$Re(CO)_5X$, X = Cl. Br	Valence level multi atom resonance	[59]
$CrCl_3$, $CrBr_3$	Core and valence level PES	[60]
WSe_2	Study of photovoltaic property using PES	[61]
$MoTe_2$, $MoSe_2$, MoS_2	Angle resolved PES in CFS mode	[62,63]
SnO_2	High resolution PES studies to probe gas sensing property	[64]
$GdCu_2$, Gd_5Si_4	Multiple atom resonance	[65]
PtSi	Electronic structure elucidation	[66]
Small molecules		
SO	Vibrational structure in the valence band region	[67]
OCS	Superexcited states by two-dimensional PES	[68]
N_2	Vibrational structure in the valence band region	[69]
SF_6	Shape resonance in the valence band region	[70–72]
Ar	Angle resolved PES	[73]
HI	High resolution threshold PES	[74]
BF_3	High resolution threshold PES, study of shape resonance	[76]
H_2S	Double photoionization studies of H_2S	[75]
CF_4, CO	Chemical effect on the carbon 1s hole-state lifetime	[77]
NH_3, ND_3, PF_3	Study of PES cross-sections and electronic structure	[78]
HF, DF	Threshold PES in the inner valence ionization region	[79]
NO	Angle and spin resolved PES	[80,81]
SO_2, CS_2	Two dimensional PES to study superexcitation and decay	[82]
HBr, DBr, Br_2, CH_3Br, CF_3Br	High resolution PES at the Br 3d edge	[83]
XeF_x, $x = 2, 4, 6$	High resolution Xe 4d PES	[84]
CS	CIS spectroscopy, study of vibrational features	[85]
NO_2^+	Vibrational structure in the valence band region	[86]
ICl	High resolution valence level PES	[87]
HCl, DCl, HI	High resolution valence band PES	[79,88]
Fe	Fe 2p and 3p photoemission magnetic dichroism	[89,90]
Ni	Resonance enhancement of satellites in the valence region, core level PES	[91,92]
Pr	Electronic structure elucidation	[93]
Ca	Shake up states in laser excited aligned Ca atoms	[94–96]
Ag	Study of shake up satellites and core hole dynamics	[97]
Pu	5f resonance photoemission	[98]
Gd	Photon energy dependence of photoemission	[99]
Lu	5p multiplet structure using PES	[100]
Ba	High resolution 4d and 5p PES	[101]
CsCl, BaF_2	Resonance enhancement of satellites in the valence region	[102]

also dependent on the angle of incident radiation and electron emission.

The MARPE phenomenon is presently described by an extension of the intra-atomic single atom resonant photoemission model described in Section 3 [104]. Considering the example of MnO, the important interactions are: (i) the dipole excitation of the O 1s photoelectron by the incident light polarization, (ii) the excitation of the $Mn2p_{3/2}$ electron to the first unoccupied Mn 3d level, and (iii) the autoionization of the excited Mn 3d state to give a free electron (same energy as the photoelectron created in (i) by the coulomb interaction coupling the Mn and O electrons. The first two

terms are one-electron matrix elements while the coulomb term is a two-electron matrix element. A recently developed more extensive model which includes covalent bonding effects as well as the multiple scattering of the incoming radiation, the many electron wave functions for the dipole and coulomb matrix elements, polarization of the electron and hole generated and configuration interaction provides a better simulation of the experimental result [103,105].

Since the core binding energies are characteristic of an atom, the presence of these resonances provides a direct probe of the near-neighbor atom. The sensitivity of MARPE effects to bonding types and distances is potentially an important spectroscopic method for various applications in inorganic and bioinorganic systems. This methodology could be used to study oxygen bound to metal surfaces and to metal ions in inorganic complexes, which have been challenging to study due to the ubiquitous presence of absorbed water.

MARPE effects have also been explored at the valence level [59]. Since there is strong mixing of the metal and ligand-based orbitals at the valence level, the interpretation of enhancements is not straightforward.

5.1.2. Vibrational fine structure in PES

Vibrational structure in core level PES was first resolved in the C 1s spectrum of methane in 1984 by Gelius et al. using the Al Kα source [106,107]. The limitation of using the Al Kα source for resolving vibrational structure was the incident radiation bandwidth (>0.3 eV). With the use of synchrotron radiation, which is characterized by high monochromacity (bandwidth <0.1 eV) and intensity, it is now possible to better resolve vibrational features and also to study the intensity changes of vibrational bands as a function of incident energy (vibrational cross-sections). Synchrotron radiation has been used to resolve vibrational features in the core and valence band region.

Vibrational structures are observed in core level PES because of the difference in the equilibrium nuclear geometry of the initial and the final (the ionized) state. The initial state is the ground vibrational state of the ground electronic state. Due to the change in the final ionized state rearranges to a different equilibrium nuclear geometry. This results in overlap between the ground vibrational level of the initial electronic state ($v'' = 0$) and a number of vibrational levels of the final electronic state ($v' = 0, 1, 2, \ldots, n$). The relative intensities of the vibrational bands are given by the Franck Condon factors (square of the overlap integral between vibrational levels of the initial and final electronic state). When the vibrational features are well resolved in the PES spectrum the energies of the vibrational levels is obtained from the spectrum, which provides insight into the potential energy surface of the final state. When the vibrational features are not well resolved, the 'equivalent core' model is usually used to approximate the energies and other parameters of the vibrational bands and is then correlated to the experimental spectrum. This model suggests that the properties of the final state (core-hole state) are similar to a molecule in which the core-ionized atom (Z) is replaced by one with an additional proton ($Z+1$), (vide infra).

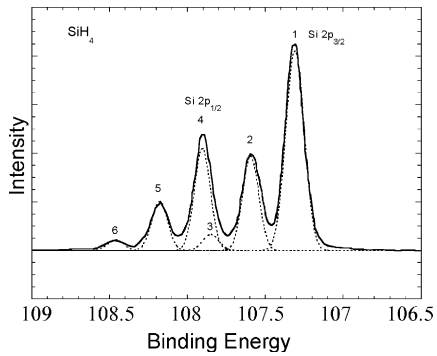

Fig. 23. Si 2p photoelectron spectrum of SiH_4. The dotted lines in the spectrum represent contributions from each vibrational and spin orbit quantum state (adapted from reference [108]).

An extensive study of the core level vibrational fine structure in the Si 2p photoelectron spectra in a series of silicon containing molecules was done by Sutherland et al. [108]. The series includes: SiH_xD_{4-x} ($x = 0$–4), $Si(CH_3)_x(OCH_3)_{4-x}$ ($x = 0$–4), $Si(CH_3)_x[N(CH_3)_2]_{4-x}$ ($x = 1$–4), $SiH_x[Si(CH_3)_3]_{4-x}$ ($x = 0$–4), SiH_3–CH_3, SiH_3–SiH_3, SiH_3–SiH_2–SiH_3, $Si(CH_3)_3$–$Si(CH_3)_3$, $Ge[Si(CH_3)_3]_4$, and $[Si(CH_3)_2]_6$. The experiments were done at the Aladdin Synchrotron, University of Wisconsin, Madison.

Here, we will focus on the gaseous molecule, SiH_4. Fig. 23 shows the Si 2p core level photoelectron spectrum. The spectrum is a resultant of contributions from the Si 2p spin orbit splitting and the Si-H stretching vibrations. The largest peak (1) at lowest binding energy (107.31 eV) is the Si $2p_{3/2}$ adiabatic transition and the Si $2p_{1/2}$ band (4) is separated from it by the Si 2p spin orbit splitting of 0.61 eV. These are further split into vibrational progressions, which has been assigned to the totally symmetric a_1 vibrational mode, on $2p_{3/2}$ (1, 2, 3) and on $2p_{1/2}$ (4, 5, 6) for $v' = 0$, 1, 2 with an energy spacing of 0.295 eV (2379 cm^{-1}). The third vibrational peak ($v' = 2$) can be detected only in the $Si2p_{1/2}$ series, and it overlaps with peak 4 in the $Si2p_{3/2}$ series. This vibrational frequency is similar to that of PH_4^+ (2295 cm^{-1})—the core equivalent species, which supports the use of the 'core equivalent' model for estimating vibrational frequencies. Additionally, the ratio of the SiH_4 and SiD_4 (spectrum not shown) vibrational frequency (0.719) matches the theoretical prediction from the ratio of the reduced masses of Si–H and Si–D according to $(\nu(\text{Si–D})/\nu(\text{Si–H})) = [\mu(\text{Si–H})/\mu(\text{Si–D})]^{1/2}$.

The high-resolution PES study on the series of Si compounds provided accurate adiabatic Si 2p ionization potentials and systematically compared the effects of different ligands on the vibrational manifold in the photoelectron spectra. This provides a database to interpret vibrational structure in the photoelectron spectra of other molecules, polymers and surfaces.

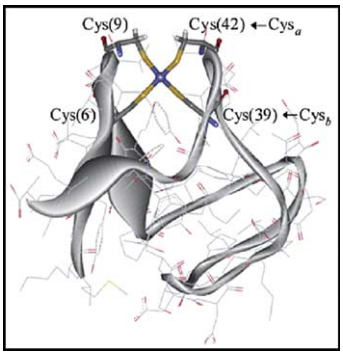

Fig. 24. Protein structure of *Desulfovibrio vulgaris* rubredoxin (1RB9). The ligands to the Fe at the active site are labeled. Cys(9) and Cys(42) are labeled Cys_a and are nearer the surface of the protein than Cys(6) and Cys(42), which are labeled Cys_b. Adapted from reference [41].

5.2. Application to bioinorganic chemistry

Application of PES to determine the electronic structure contributions to redox properties of mononuclear iron-sulfur active sites demonstrates the power of the experimental and theoretical methodology outlined in this review. Using a combination of core and valence PES data on $[Fe(SR)_4]^{2-,1-}$ model complexes, the electronic structure of the reduced and oxidized sites have been elucidated—and their contributions to the observed redox properties for such sites have been evaluated [41,109,110]. Results from these studies are used to provide key insights into the functional requirements for rapid electron transfer in the mononuclear iron–sulfur electron transfer proteins known as rubredoxins which contain $Fe^{2+/3+}$ coordinated to four Cys residues in a D_{2d} distorted T_d structure (Fig. 24).

Fe $2p_{3/2}$ PES core ionization data for $[Fe(SPh)_4]$ in the Fe(II) (reduced) and Fe(III) (oxidized) oxidation states are given in Fig. 25A. The Fe(II) complex exhibits a strong shake-up satellite (S) on the high energy side of the main peak (M) whereas the Fe(III) species exhibits only a weak satellite feature. Qualitatively, this demonstrates convincingly that there is more electronic relaxation for the

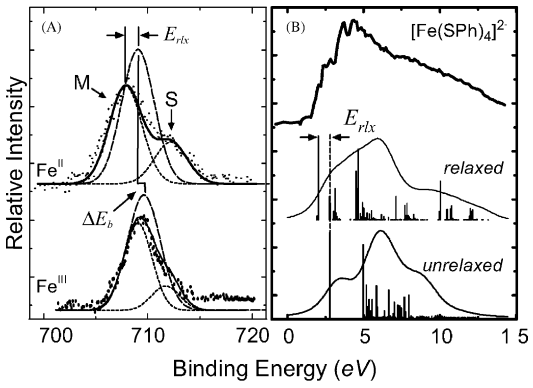

Fig. 25. (A) Core Fe $2p_{3/2}$ ionization spectra for $[Fe(SPh)_4]^{2-,1-}$ and (B) corrected valence PES spectra for $[Fe(SPh)_4]^{2-}$. Experimental details are given in reference [41].

Fe(II) → Fe(III) process than for Fe(III) → Fe(IV). The magnitude of electronic relaxation (Δq_{rlx}) can be quantified from these experimental data using the VBCI model developed in Section 4.3. As expected from the relative intensities of the satellite peaks in Fig. 25A, the amount of relaxation is significantly greater for Fe(II) → Fe(III) ($\Delta q_{rlx} \sim -0.82$) than for Fe(III) → Fe(IV) ($\Delta q_{rlx} \sim -0.40$). Notably, the large negative Δq_{rlx} for Fe(II) ionization indicates massive LMCT upon oxidation, which stabilizes the localized Fe 2p core hole. These results are very similar to those which have been observed for $[FeCl_4]^{2-,1-}$ in Section 4 [41].

These core ionization data further reveal insight into the nature of the valence redox process. The intensity-weighted average core ionization energy ($E_b^{Fe\ 2p_{3/2}}$) of the oxidized species is only 0.4 eV deeper than that for the reduced species (ΔE_b in Fig. 25A), implying that the overall difference in charge between the reduced and oxidized sites (Δq_{redox}) is very small. This has been quantified for $[Fe(SPh)_4]^{2-,1-}$ and indicates that the charge change on the iron is extremely small on oxidation; $\Delta q_{redox} \sim +0.10e$. For $[FeCl_4]^{2-,1-}$, Δq_{redox} has been calculated to be quite a bit larger ($\sim +0.2e$) indicating that there are some important quantitative differences between the redox behaviors of the tetrathiolate and the tetrachloride redox couples [41,110].

Valence PES data for $[Fe(SPh)_4]^{2-}$ are given in Fig. 25B (the normalized ratio of intensities at two different photon energies 45 and 25 eV is shown, which corrects for the contribution from the ring and the counterion). The data show the effect of atomic multiplets in the $3d^{n-1}$ final state for valence ionization processes (vide supra). VBCI simulations, including the effects of atomic multiplets, are used to determine the magnitude of electronic relaxation for valence ionization. As for the core ionization of the ferrous species, atomic multiplet simulations do not adequately account for the large observed intensity at higher binding energies (see the unrelaxed simulation in Fig. 25B); inclusion of shake-up LMCT final states allows for greater intensity distribution to higher energy and thus better agreement with experiment. From the relaxed simulations in Fig. 25B, Δq_{rlx} for valence ionization of the ferrous species is calculated to be $\sim -0.75e$, which is still very large although somewhat smaller than that calculated for core ionization. As with the core ionization data, relaxation in the tetrathiolate model is slightly greater than in the reference tetrachloride system [41,110].

In agreement with these PES results, DFT results indicate a dramatic change in the electronic structure on redox for the tetrathiolate model. As also observed in the tetrachloride, DFT-calculated redox densities indicate a dramatic shift in electron density from the ligands to the metal—compensating for the increased positive charge at the oxidized metal center. The effect of electronic relaxation is calculated to be even larger for the tetrathiolate complex than for the tetrachloride. It is reasonable to conclude that electronic relaxation is a critical aspect of the electronic structure of $[FeX_4]$ high-spin iron redox couple, which suggests that rubredoxins, a class of electron trans-

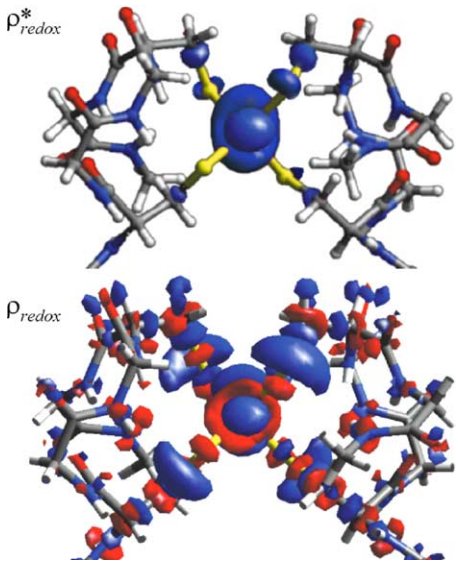

Fig. 26. Redox densities for the active site of rubredoxin. See reference [109] for details.

port proteins that have an $[Fe(SCys)_4]^{2-,1-}$ active site, should also exhibit very strong electronic relaxation. Furthermore, this electronic relaxation should have a dramatic influence on the redox properties of this electron transport protein [110].

5.2.1. Electronic relaxation effects on the ET properties of rubredoxin

Although direct PES experiments on the protein active sites were unfeasible, the protein sites are spectroscopically very similar to tetrathiolate model systems such as the one investigated above [41]. Additionally, the success of DFT in describing the electronic structure of the well-characterized $[FeX_4]^{2-,1-}$ redox couples described above strongly suggests that it would prove equally successful in elucidating the electronic structure of the protein active site. DFT calculations on a large 104-atom protein fragment that contains the complete active site (including hydrogen-bonding effects to the sulfur ligands) indicate that the overall description of the redox process is only somewhat perturbed by the active site structure and exhibits very large electronic relaxation on oxidation of the ferrous protein. The effect on the nature of the oxidation process is dramatic as evidenced by the large differences between ρ_{redox} and ρ^*_{redox} at the active site seen in Fig. 26. From our calculations, the electronic structure of the ferrous species indicates that the highest energy electron resides in a molecular orbital (the redox-active molecular orbital, RAMO) that has predominantly Fe $3d_{z^2}$ character (∼85%). This description of the ferrous site is highly consistent with available spectroscopic data on rubredoxins and model systems [111–113]. Allowing for electronic relaxation results in dramatic changes in the nature of the redox-active electron (see ρ_{redox} in Fig. 26) even though the RAMO itself changes only slightly. Electronic relaxation allows for changes in the passive electrons to compensate for the loss of the metal-based electron. These changes increase the ligand contribution to the ionization process such that the overall ionization occurs mostly (∼90%) on the ligands. Electronic relaxation therefore transfers significant charge from the ligands to the metal to stabilize the electron-deficient metal center on oxidation. The large calculated Δq_{rlx} for the Rd model ($\Delta q_{rlx} \sim -0.72$e) is in good agreement with the experimentally and theoretically-derived values that have been obtained for $[Fe(SPh)_4]^{2-,1-}$. In fact, DFT results on a series of geometric perturbations of the $[Fe(SR)_4]^{2-,1-}$] unit suggest that the magnitude of electronic relaxation for these systems is quite insensitive to small differences in the ground state electronic structure that are known to exist between Rd and model systems [109].

Electronic contributions to the reduction potentials are directly related to the vertical ionization energies (I_{vert}) obtained from PES experiments on the reduced species. As discussed above, electronic relaxation redistributes intensity into LMCT final states, which decrease the energy of the initial ionization peak by stabilizing the final state through charge redistribution. The energy stabilization of the main peak through relaxation (E_{rlx}) is therefore the energy difference between the binding energy of the main peak and that of the unrelaxed final state. As described previously in Section 4.3, VBCI simulations provide a method of calculating E_{rlx}, a measure of the stabilization of the oxidized site due to electronic relaxation. This stabilization translates directly to a decrease in the reduction potential, i.e. making it easier to oxidize the reduced species. From the shift in the valence ionization energy of $[Fe(SPh)_4]^{2-}$ due to electronic relaxation (see Fig. 25B), we see that E^{RAMO}_{rlx} is ∼0.6 eV, which is a significant stabilization. In the protein, this effect will be somewhat modulated by the protein matrix, but the overall magnitude of the stabilization would remain similar. Thus for rubredoxins, a significant effect of electronic relaxation would be to decrease the reduction potentials from ∼0.5 V to experimentally observed potentials near 0 V [109,110,114–120].

In addition to the large effect on the thermodynamics of electron transfer, electronic relaxation exhibits a dramatic influence on the magnitude of geometric changes that occur on the redox properties of $[FeX_4]^{2-,1-}$ complexes and thus exerts a strong influence on the kinetics of electron transfer through its inner-sphere reorganization energy (λ_i). To explore this issue, DFT potential energy surfaces for $[Fe(SCH_3)_4]^{2-,1-}$ were constructed as given in Fig. 27. As observed experimentally, the equilibrium bond distance (r_{eq}) is slightly greater for the reduced species ($\Delta r_{redox} = r_{eq}(red) - r_{eq}(ox) \sim 0.03$ Å). Without electronic relaxation, however, the potential energy surface for the oxidized species (Fe^{3+}) differs substantially and predicts a much shorter equilibrium bond distance. From this, we find that an important consequence of electronic relaxation is a smaller Δr_{redox} resulting from a decrease of the electrostatic distorting force for bond contraction. This effect has a stunning impact on λ_i, which

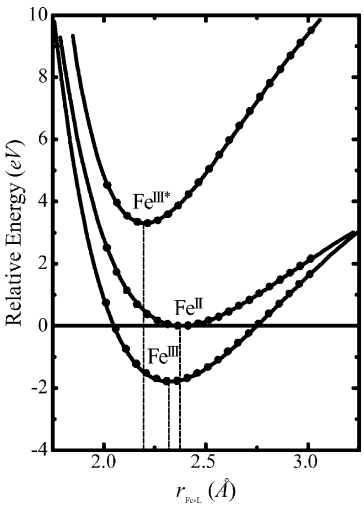

Fig. 27. DFT potential energy surfaces for $[Fe(SCH_3)_4]^{2-,1-}$. Reproduced from reference [109].

is calculated to decrease by nearly 1 eV when electronic relaxation is allowed to occur [109].

A similar analysis has been performed for the active site of rubredoxin. Again, the calculated bond distance changes are larger ($\Delta r^*_{redox} \sim 0.06$ Å) if electronic relaxation is suppressed than if the electronic structure is allowed to relax ($\Delta r_{redox} \sim 0.03$ Å) on valence ionization. The effect on bond distances is more modest than in the model system, but the effect on reorganization energies is just as large: λ_i is calculated to decrease from ~1.2 to only 0.2 eV due to electronic relaxation. As shown from DFT-calculated potential energy surfaces of the $[FeX_4]^{2-,1-}$ model systems, electronic relaxation effectively reduces the electrostatic distorting force that contracts the Fe–S bonds by decreasing the Coulomb attraction between the negatively-charged ligands and the positively-charged metal through redistribution of the electron density in the oxidized state. This results in a very small Δr_{redox}, which translates into a very small inner-sphere contribution to the reorganization energy for electron transfer [110].

Lastly, electronic relaxation also influences the magnitude of coupling between the donor and acceptor orbitals during redox processes (H_{DA}). This influence, as first described by Newton [121] for six-coordinate iron systems, is relatively small and does not significantly affect the overall kinetics of electron transfer. Relaxation-corrected estimates for H_{DA} have been used to investigate the possible electron transfer pathways in this protein, and it has been shown that only a few pathways can lead to efficient electron transfer to/from the active site, as indicated in Fig. 28. For electron self-exchange reactions, direct overlap of the two slightly buried metal centers is statistically unlikely—an efficient superexchange pathway through the two surface-accessible cysteine ligands is therefore the dominant route to the surface of the protein. A series of secondary pathways also contribute because of hydrogen bonding between the four

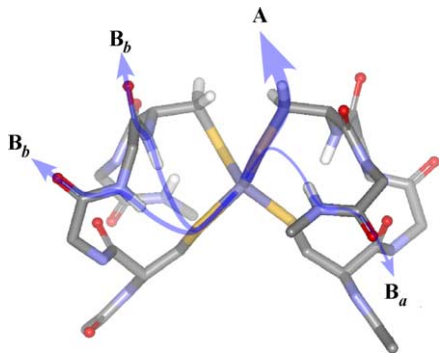

Fig. 28. Important electron pathways for rubredoxins as calculated for the electron self-exchange reaction. Reproduced from reference [109].

ligated sulfur atoms and surface-accessible backbone amide groups. The contribution from these secondary pathways has been estimated at ~20% of the total electron self-exchange rate [109].

Taken together, the influence of electronic relaxation on λ_i and H_{DA} has a profound effect on the expected rates of electron transfer that can be achieved by rubredoxins. The dominant effect is the substantial decrease in inner-sphere reorganization energy (~1 eV), which translates into an effective increase in rate for rubredoxin self-exchange (k_{ese}) from a rather plodding 10^3 M^{-1} s^{-1} to the rather more effective 10^6 M^{-1} s^{-1}—an incredible three order of magnitude increase in the rate of self-exchange!

Therefore, core and valence PES studies coupled with parallel DFT calculations on a well-characterized iron sulfur redox couple has provided significant insight into the fundamental electronic structure contributions to the redox properties of a biologically important electron transfer protein active site. The cysteine ligands provide impressive stabilization of the oxidized site (by 0.5 V) through increased charge donation in the ferric site. This redistribution of charge density between the metal and ligands also minimizes geometric changes associated with the redox process and efficiently decreases the inner-sphere reorganization energy (by ~1 eV), leading to biologically efficient electron transfer to and from the active site of rubredoxins.

6. Concluding remarks

Variable energy PES has revolutionized ones ability to assign and analyze the photoelectron spectra of transition metal complexes. Rather than correlating a molecular orbital calculation (often based on Koopmans' theorem) to the HeI or HeII photoelectron spectrum, or chemically perturbing the system to look for shifts in PES peaks, the intensity dependence of a PES spectrum with change in synchrotron photon energy defines the nature of the orbitals being ionized and allows a quantitative estimate of their covalent mixings through photoionization cross-section effects. Through shake up satellites or resonance effects at edges, one can

further probe electronic relaxation, the change in electronic structure due to ionization. This can be quantified through a VBCI model, which is strongly supported by DFT calculations. Electronic relaxation is found to be very large for transition metal complexes due to the large change in metal centered electron–electron repulsion upon ionization and must be included in any reasonable analysis. The large electronic relaxation observed in the valence region emphasizes the importance of this effect in transition metal chemistry including inorganic redox processes, where electronic relaxation can lower potentials and raise rates of ET through lowering the reorganization energy.

Acknowledgements

EIS wishes to thank his students and collaborators as cited in the references for their key contributions to their research. This work was supported by NSF CHE-9980549 (E.I.S.). SSRL operations are funded by the Department of Energy, Office of Basic Energy Sciences.

References

[1] K. Siegbahn, Alpha, Beta, and Gamma-Ray Spectroscopy, Amsterdam, North Holland, 1965.
[2] K. Siegbahn, C. Nordling, A. Fahlman, R. Nordberg, K. Hamrin, J. Hedman, G. Johansson, T. Bergmark, S.E. Karlsson, I. Lindgren, B. Lindberg, ESCA, Atomic, Molecular and Solid State Structure by Means of Electron Spectroscopy, Almqvist and Wiksell, Uppsala, 1967.
[3] K. Siegbahn, C. Nordling, J. Johansson, J. Hedman, P.F. Heden, K. Hamrin, U. Gelius, T. Bergmark, L.O. Werme, R. Manne, Y. Baer, ESCA Applied to Free Molecules, Amsterdam, North Holland, 1969.
[4] D.W. Turner, M.I. Al-Joboury, J. Chem. Phys. 37 (1963) 3007.
[5] M.O. Krause, Phys. Rev. A 140 (1965) 1845.
[6] B.L. Kurbatov, F.I. Viselov, Sov. Phys. Dokl. 6 (1962) 1091.
[7] J.W. Rabalais, Principles of Ultraviolet Photoelectron Spectroscopy, Wiley, New York, 1977.
[8] A.W. Potts, H.J. Lempka, D.G. Streets, W.C. Price, Phil. Trans. R. Soc. Lond. 268 (1970) 59.
[9] H. Winick, S. Doniach (Eds.), Synchrotron Radiation Research, Plenum Press, New York, 1980.
[10] H. Saisho, Y. Gohshi (Eds.), Applications of Synchrotron Radiation to Materials Analysis, vol. 7, Elsevier Science, Amsterdam, 1996.
[11] V. Saile, Nucl. Instrum. Methods 152 (1978) 59.
[12] F.C. Brown, R.Z. Bachrach, L. N, Nucl. Instrum. Methods 152 (1978) 73.
[13] W. Eberhardt, G. Kalkoffen, C. Kunz, Nucl. Instrum. Methods 152 (1978) 81.
[14] S. Doniach, I. Lindau, W.E. Spicer, H. Winick, J. Vac. Sci. Technol. 12 (1975) 1123.
[15] R. Spohr, E.V. Puttkamer, Naturforsch 22 (1967) 409.
[16] D.C. Frost, C.A. MacDowell, D.A. Wroom, Proc. R. Soc., Ser. A 296 (1967) 566.
[17] P.H. Citrin, R.W.S. Jr., T.D. Thomas, Electron Spectroscopy, North Holland, Amsterdam, 1972, p. 105.
[18] L. Heroux, H.E. Hinteregger, Rev. Sci. Instrum. 31 (1960) 280.
[19] A.A. Gewirth, S.L. Cohen, H.J. Schugar, E.I. Solomon, Inorg. Chem. 26 (1987) 1133.
[20] D.C. Frost, A. Ishitani, C.A. McDowell, Mol. Phys. 24 (1972) 861.
[21] R. Manne, T. Aberg, Chem. Phys. Lett. 7 (1970) 282.
[22] J.H. van Vleck, Phys. Rev. 35 (1934) 405.
[23] D.A. Shirley, in: M. Cardona, L. Ley (Eds.), Photoemission in Solids, vol. I, Springer Verlag, Berlin, 1978.
[24] T. Koopmans, Physica 1 (1933) 104.
[25] S.M. Goldberg, C.S. Fadley, S. Kono, J. Electron. Spec. Relat. Phen. 21 (1981) 285.
[26] E.W. Plummer, W. Eberhardt, Adv. Chem. Phys. 49 (1983) 533.
[27] E.W. Plummer, T. Gustafsson, Science 198 (1977) 165.
[28] M.J. Sayers, M.R. McClellan, R.R. Gay, E.I. Solomon, F.R. McFeely, Chem. Phys. Lett. 75 (1980) 575.
[29] M.R. McClellan, M. Trenary, N.S. Shinn, M.J. Sayers, K.L. D'Amico, E.I. Solomon, F.R. McFeely, J. Chem. Phys. 74 (1981) 4726.
[30] K.L. D'Amico, M. Trenary, N.S. Shinn, E.I. Solomon, F.R. McFeely, J. Am. Chem. Soc. 104 (1982) 5102.
[31] U. Fano, J.W. Cooper, Rev. Mod. Phys. 40 (1968) 441.
[32] S.T. Manson, in: M. Cardona, L. Ley (Eds.), Photoemission in Solids, vol. I, Springer Verlag, Berlin, 1978.
[33] D.E. Eastman, M. Kuznietz, J. Appl. Phys. 42 (1971) 1396.
[34] J.J. Yeh, I. Lindau, At. Data Nucl. Data Tables 32 (1985) 1.
[35] S.V. Didziulis, S.L. Cohen, A.A. Gewirth, E.I. Solomon, J. Am. Chem. Soc. 110 (1988) 250.
[36] U. Gelius, K. Siegbahn, Faraday Discuss. Chem. Soc. 54 (1972) 257.
[37] U. Gelius, in: D.A. Shirley (Ed.), Electron Spectroscopy, North Holland, Amsterdam, 1972.
[38] L.C. Davis, Phys. Rev. B 25 (1982) 2912.
[39] L.C. Davis, L.A. Feldkamp, Phys. Rev. B 23 (1981) 6239.
[40] The CFS spectrum is obtained by scanning the photon energy while analyzing electrons in the secondary electron peak. This is basically a partial electron yield absorption spectrum.
[41] P. Kennepohl, E.I. Solomon, Inorg. Chem. 42 (2003) 679.
[42] K.D. Butcher, S.V. Didziulis, B. Briat, E.I. Solomon, Inorg. Chem. 29 (1990) 1626.
[43] K.D. Butcher, S.V. Didziulis, B. Briat, E.I. Solomon, Inorg. Chem. 112 (1990) 2231.
[44] The satellite features are clearer in the Rb salt, since the Rb 4p peaks do not obscure the satellite region.
[45] K. Okada, A. Kotani, B.T. Thole, G.A. Sawatzky, Solid State Communications 76 (1990) 1277.
[46] K. Okada, A. Kotani, B.T. Thole, J. Electr. Spectrosc. Relat. Phenom. 58 (1992) 325.
[47] C. Angeli, C. Berthier, G. Rolando, S.M.C. Alcaraz, O. Dutuit, J. Phys. Chem. A 101 (1997) 7909.
[48] M. Tsunekawa, S. Suga, T. Matsushita, T. Muro, S. Ueda, H. Daimon, S. Imada, T. Nakatani, Y. Saitoh, T. Iwasaki, A. Sekiyama, A. Fuyimori, H. Ishii, T. Miyahara, T. Hanyu, H. Namatame, M. Taniguchi, E. Shigemasa, O. Sakai, R. Takayama, R. Settai, H. Azuma, Y. Onuki, Solid State Communications 103 (1997) 659.
[49] A. Kikas, E. Nommiste, R. Ruus, A. Saar, I. Martinson, Solid State Communications 115 (2000) 275.
[50] S.A. Morton, G.D. Waddill, S. Kim, I.K. Schuller, S.A. Chanbers, J.G. Tobin, Surf. Sci. 513 (2002) L451.
[51] X.R. Li, G.M. Bancroft, R.J. Puddephatt, Z.F. Liu, K.H. Tan, J. Am. Chem. Soc. 116 (1994) 9543.
[52] X.R. Li, G.M. Bancroft, R.J. Puddephatt, Y.F. Hu, K.H. Tan, Organometallics 15 (1996) 2890.
[53] Y.F. Hu, G.M. Bancroft, K.H. Tan, Inorg. Chem. 39 (2000) 1255.
[54] J.C. Wu, G.M. Bancroft, R.J. Puddephatt, Y.F. Hu, X.R. Li, K.H. Tan, Inorg. Chem. 38 (1999) 4688.
[55] X.R. Li, J.S. Tse, G.M. Bancroft, R.J. Puddephatt, K.H. Tan, Inorg. Chem. 35 (1996) 2515;
C.N. Field, J.C. Green, M. Mayer, V.A. Nasluzov, N. Rosch, M.R.F. Siggel, Inorg. Chem. 35 (1996) 2504.
[56] X.R. Li, J.S. Tse, G.M. Bancroft, R.J. Puddephatt, K.H. Tan, Organometallics 14 (1995) 4513.

[57] Y.F. Hu, G.M. Bancroft, H.B. Davis, J.I. Male, R.K. Pemeroy, J.S. Tse, K.H. Tan, Organometallics 15 (1996) 4493.
[58] Y.F. Hu, G.M. Bancroft, K.H. Tan, J.S. Tse, D.S. Yang, Can. J. Chem. 74 (1996) 2240.
[59] Y.F. Hu, G.M. Bancroft, K.H. Tan, J. Electr. Spectrosc. Relat. Phenom. 114–116 (2001) 147.
[60] I. Pollini, Solid State Communications 106 (1998) 549.
[61] A. Klein, Y. Tomm, R. Schlaf, C. Pettenkofer, W. Jaegermann, M. LuxSteiner, E. Bucher, Solar Energy Mater. Solar Cells 51 (1998) 181.
[62] T. Boker, A. Muller, J. Augustin, C. Janowitz, R. Manzke, Phys. Rev. B 60 (1999) 4675.
[63] T. Boker, R. Severin, A. Muller, C. Janowitz, R. Manzke, D. Voss, P. Kruger, A. Mazur, J. Pollmann, Phys. Rev. B 64 (2001) 235305.
[64] M. Sinner-Hettenbach, N. Barsan, U. Weimer, T. Weiss, H. van Schenk, M. Gothelid, L. Giovanelli, G. LeLay, Thin Solid Films 391 (2001) 192.
[65] J. Szade, G. Skorek, M. Neumann, B. Schneider, F. Fangmeyer, A. Matteucci, G. Paolucci, A. Goldoni, Surf. Sci. 497 (2002) 29.
[66] N. Franco, J.E. Klepeis, C. Bostedt, T. Van Buuren, C. Heske, O. Pankratov, L.J. Terminello, J. Electr. Spectrosc. Relat. Phenom. 114 (2001) 1191.
[67] J.M. Dyke, D. Haggerston, A. Morris, S. Stranges, J.B. West, T.G. Wright, A.E. Wright, J. Chem. Phys. 106 (1997) 821.
[68] Y. Hikosaka, H. Hattori, T. Hikida, K. Mitsuke, J. Chem. Phys. 107 (1997) 2950.
[69] H. Yoshii, T. Tanaka, Y. Morioka, T. Hayaishi, R.I. Hall, J. Mol. Spectrosc. 186 (1997) 155.
[70] A.J. Yencha, M.C.A. Lopes, D.B. Thompson, G.C. King, J. Phys. B At. Mol. Opt. Phys. 33 (2000) 945.
[71] A.J. Yencha, D.B. Thompson, A.J. Cormack, D.R. Cooper, M. Zubek, P. Bolognesi, G.C. King, Chem. Phys. 216 (1997) 227.
[72] S.W.J. Scully, R.A. Mackie, R. Browning, K.F. Dunn, C.J. Latimer, J. Phys. B At. Mol. Opt. Phys. 35 (2002) 2703.
[73] K. Mitsuke, Y. Hikosaka, T. Iwasaki, J. Phys. B At. Mol. Opt. Phys. 33 (2000) 391.
[74] A.J. Cormack, A.J. Yencha, R.J. Donovan, K.P. Lawley, A. Hopkirk, G.C. King, Chem. Phys. 221 (1997) 175.
[75] J.H.D. Eland, P. Lablanquie, M. Lavollee, M. Simon, R.I. Hall, M. Hochlaf, F. Penent, J. Phys. B At. Mol. Opt. Phys. 30 (1997) 2177.
[76] A.J. Yencha, M.C.A. Lopes, G.C. King, Chem. Phys. 279 (2002) 55.
[77] T.X. Carroll, K.J. Borve, L.J. Saethre, J.D. Bozek, E. Kukk, J.A. Hanhe, T.D. Thomas, J. Chem. Phys. 116 (2002) 10221.
[78] D. Edvardsson, P. Baltzer, L. Karlsson, B. Wannberg, D.M.P. Holland, D.A. Shaw, E.E. Rennie, J. Phys. B At. Mol. Opt. Phys. 32 (1999) 2583;
J.C. Green, N. Kaltsoyannis, K.H. Sze, M.A. Macdonald, J. Chem. Soc. Dalton Trans. 9 (1991) 2371.
[79] A.J. Yencha, M.C.A. Lopes, M.A. MacDonald, G.C. King, Chem. Phys. Lett. 310 (1999) 433.
[80] S.C. Kuo, Z.Y. Zhang, S.K. Ross, R.B. Klemm, R.D. Johnson, P.S. Monks, R.P. Thorn, L.J. Stief, J. Phys. Chem. A 101 (1997) 4035.
[81] M. Salzmann, A. Muller, N. Bowering, U. Heinzmann, J. Phys. B At. Mol. Opt. Phys. 32 (1999) 2517.
[82] K. Mitsuke, H. Hattori, Y. Hikosaka, J. Electr. Spectrosc. Relat. Phenom. 112 (2000) 137.
[83] J. Johnson, J.N. Cutler, G.M. Bancroft, Y.F. Hu, K.H. Tan, J. Phys. B At. Mol. Opt. Phys. 30 (1997) 4899.
[84] J.N. Cutler, G.M. Bancroft, J.D. Bozek, K.H. Tan, G.J. Schrobilgen, J. Am. Chem. Soc. 113 (1991) 9125.
[85] J.M. Dyke, S.D. Gamblin, D. Haggerston, A. Morris, S. Stranges, J.B. West, T.G. Wright, A.E. Wright, J. Chem. Phys. 108 (1998) 6258.
[86] G.K. Jarvis, Y. Song, C.Y. Ng, E.R. Grant, J. Chem. Phys. 111 (1999) 9568.
[87] A.J. Yencha, M.C.A. Lopes, G.C. King, Chem. Phys. Lett. 325 (2000) 559.
[88] A.J. Yencha, A.J. Cormack, R.J. Donovan, A. Hopkirk, G.C. King, Chem. Phys. 238 (1998) 109.
[89] G. Panaccione, F. Sirotti, S. Lizzit, A. Baraldi, G. Paolucci, N.A. Cherepkov, G. Rossi, Surf. Sci. 377 (1997) 440.
[90] F.O. Schumann, J.G. Tobin, Surf. Sci. 476 (2001) L235.
[91] K. Ono, A. Kakizaki, T. Tanaka, K. Shimada, Y. Saitoh, T. Sendohda, Solid State Communications 101 (1997) 739.
[92] H.W. Nesbitt, D. legrand, G.M. Bancroft, Phys. Chem. Miner. 27 (2000) 357.
[93] C.Y. Hwang, J.W. Lee, S.T. Kim, D.H. Lee, M. Onellion, Solid State Communications 103 (1997) 229.
[94] M. Wedowski, K.W. Godehusen, F.P. Zimmermann, M. Martins, T. Dohrmann, A. vondemBorne, B. Sonntage, A.N. GrumGrzhimailo, Phys. Rev. A 55 (1997) 1922.
[95] A. Gottwald, S. Anger, J.M. Bizau, D. Rosenthal, M. Richter, Phys. Rev. A 55 (1997) 3941.
[96] P. Wernett, P. Glatzel, A. Verweyen, B. Sonntag, B. Obst, W. Benten, C. Gerth, P. Zimmermann, A. Gray, J. Costello, J. Phys. B At. Mol. Opt. Phys. 31 (1998) L289.
[97] J. Morais, A. deSiervo, R. Landers, S.G.C. deCastro, M. Abbate, G.G. Kleiman, J. Electr. Spectrosc. Relat. Phenom. 103 (1999) 661.
[98] J. Terry, R.K. Schulze, J.D. Farr, T. Zocco, K. Heinzelman, E. Rotenberg, D.K. Shuh, G. Vanderlaan, D.A. Arena, J.G. Toben, Surf. Sci. 499 (2002) L141.
[99] J. Szade, M. Neumann, I. Karla, B. Schneider, F. Fangmeyer, M. Matteucci, Solid State Communications 113 (2000) 709.
[100] C. Gerth, M. Martins, S. Brunken, K. Godehusen, B. Kanngiesser, P. Zimmermann, J. Phys. B At. Mol. Opt. Phys. 32 (1999) L133.
[101] G. Snell, M. Martins, E. Kukk, W.T. Chen, N. Berrah, Phys. Rev. 63 (2001) 62715.
[102] M. Kamada, M. Itoh, Phys. Rev. 65 (2002) 245104.
[103] A.W. Kay, F.J. Garcia de Abajo, S.H. Yang, E. Arenholz, B.S. Mun, N. Mannella, Z. Hussain, M.A. Van Hove, C.S. Fadley, Phys. Rev. B 63 (2001) 115119.
[104] A.W. Kay, E. Arenholz, B.S. Mun, N. Mannella, F.J. Garcia de Abajo, C.S. Fadley, R. Denecke, Z. Hussain, M.A. Van Hove, Science 281 (1998) 679.
[105] F.J. Garcia de Abajo, C.S. Fadley, M.A. Van Hove, Phys. Rev. Lett. 82 (1999) 4126.
[106] U. Gelius, S. Svensson, H. Seigbahn, E. Basilier, A. Faxlav, K. Seigbahn, Chem. Phys. Lett. 28 (1974) 1.
[107] U. Gelius, L. Asplund, E. Basilier, K. Helenelund, H. Seigbahn, Nucl. Instrum. Methods B 229 (1984) 85.
[108] D.G. Sutherland, G.M. Bancroft, K.H. Tan, J. Chem. Phys. 97 (1992) 7918.
[109] P. Kennepohl, E.I. Solomon, Inorg. Chem. 42 (2003) 696.
[110] P. Kennepohl, E.I. Solomon, Inorg. Chem. 42 (2003) 689.
[111] M.S. Gebhard, S.A. Koch, M. Millar, F.J. Devlin, P.J. Stephens, E.I. Solomon, J. Am. Chem. Soc. 113 (1991) 1640.
[112] M.S. Gebhard, J.C. Deaton, S.A. Koch, M. Millar, E.I. Solomon, J. Am. Chem. Soc. 112 (1990) 2217.
[113] W. Lovenberg (Ed.), Iron Sulfur Proteins, vol. I–III, Academic Press, New York, 1973.
[114] P.J. Stephens, D.R. Jollie, A. Warshel, Chem. Rev. 96 (1996) 2491.
[115] R. Kummerle, H. Zhuang-Jackson, J. Gaillard, J.-M. Moulis, Biochemistry 36 (1997) 15983.
[116] D.W. Low, M.G. Hill, J. Am. Chem. Soc. 122 (2000) 11039.
[117] D.W. Low, M.G. Hill, J. Am. Chem. Soc. 120 (1998) 11536.
[118] Z.G. Xiao, M.J. Maher, M. Cross, C.S. Bond, G.J.M.A.G. Wedd, J. Biol. Inorg. Chem. 5 (2000) 75.
[119] M.K. Eidsness, A.E. Burden, K.A. Richie, D.M. Kurtz, R.A. Scott, E.T. Smith, T. Ichiye, B. Beard, T.P. Min, C.H. Kang, Biochemistry 38 (1999) 14803.
[120] M.K. Eidsness, A.E. Burden, K.A. Richie, D.M. Kurtz, R.A. Scott, E.T. Smith, T. Ichiye, B. Beard, T.P. Min, C.H. Kang, Biochemistry 39 (2000) 626.
[121] M.D. Newton, Int. J. Quantum Chem. 77 (2000) 255.